



Defense Threat Reduction Agency
8725 John J. Kingman Road, MS 6201
Fort Belvoir, VA 22060-6201



DTRA-TR-01-21

TECHNICAL REPORT

Density Imaging Diagnostic for Plasma Radiation Sources

Approved for public release; distribution is unlimited.

August 2005

20050907 019

DSWA01-96-C-0172

Edward J. Yadlowsky, et al.

Prepared by:
HY-Tech Research Corporation
104 Centre Court
Radford, VA 24141

DESTRUCTION NOTICE

FOR CLASSIFIED documents, follow the procedures in DoD 5550.22-M, National Industrial Security Program Operating Manual, Chapter 5, Section 7 (NISPOM) or DoD 5200.1-R, Information Security Program Regulation, Chapter 1X.

FOR UNCLASSIFIED limited documents, destroyed by any method that will prevent disclosure of contents or reconstruction of the document.

Retention of this document by DoD contractors is authorized in accordance with DoD 5220.22-M, Industrial Security Manual.

PLEASE NOTIFY THE DEFENSE THREAT REDUCTION AGENCY, ATTN: BDLMI, 8725 JOHN J. KINGMAN ROAD, MS-6201, FT BELVOIR, VA 22060-6201, IF YOUR ADDRESS IS INCORRECT, IF YOU WISH IT DELETED FROM THE DISTRIBUTION LIST, OR IF THE ADDRESSEE IS NO LONGER EMPLOYED BY YOUR ORGANIZATION.

DISTRIBUTION LIST UPDATE

This mailer is provided to enable DTRA to maintain current distribution lists for reports. (We would appreciate you providing the requested information.)

- ☐ Add the individual listed to your distribution list.
- ☐ Delete the cited organization/individual.
- ☐ Change of address.

Note:

Please return the mailing label from the document so that any additions, changes, corrections or deletions can be made easily. For distribution cancellation or more information call DTRA/BDLMI (703) 767-4725.

NAME: _____

ORGANIZATION: _____

OLD ADDRESS

NEW ADDRESS

TELEPHONE NUMBER: () _____

DTRA PUBLICATION NUMBER/TITLE

CHANGES/DELETIONS/ADDITONS, etc.
(Attach Sheet if more Space is Required)

DTRA or other GOVERNMENT CONTRACT NUMBER: _____

CERTIFICATION of NEED-TO-KNOW BY GOVERNMENT SPONSOR (if other than DTRA):

SPONSORING ORGANIZATION: _____

CONTRACTING OFFICER or REPRESENTATIVE: _____

SIGNATURE: _____

DEFENSE THREAT REDUCTION AGENCY
ATTN: BDLMI
8725 John J Kingman Road, MS 6201
Fort Belvoir, VA 22060-6201

DEFENSE THREAT REDUCTION AGENCY
ATTN: BDLMI
8725 John J Kingman Road, MS 6201
Fort Belvoir, VA 22060-6201

REPORT DOCUMENTATION PAGE			Form Approved	
Public reporting burden for this collection of information is estimated to average 1 hour per response, including the time for reviewing instructions, searching existing data sources, gathering and maintaining the data needed, and completing and reviewing the collection of information. Send comments regarding this burden, estimate or any other aspect of this collection of information, including suggestions for reducing this burden, to Washington Headquarters Services, Directorate for Information Operations and Reports, 1215 Jefferson Davis Highway, Suite 1204, Arlington, VA 22202-4302, and to the Office of Management and Budget, Paperwork Reduction Project (0704-0188), Washington, DC 20503.				
1. AGENCY USE ONLY (Leave blank)		2. REPORT DATE 050800		3. REPORT TYPE AND DATES COVERED Technical 960910 - 990810
4. TITLE AND SUBTITLE Density Imaging Diagnostic for Plasma for Plasma Radiation Sources			5. FUNDING NUMBERS C - DSWA01-96-C-0172 PE - 462D PR - AB TA - WU - DH 00999	
6. AUTHOR(S) Edward J. Yadlowsky, Eric Carlson, Farid Barakat, and Robert C. Hazelton				
7. PERFORMING ORGANIZATION NAME(S) AND ADDRESS(ES) HY-Tech Research Corporation 104 Centre Court Radford, VA 24141			8. PERFORMING ORGANIZATION REPORT NUMBER	
9. SPONSORING/MONITORING AGENCY NAME(S) AND ADDRESS(ES) Defense Threat Reduction Agency 8725 John J. Kingman Road, STOP-6201 Fort Belvoir, VA 22060-6201 TDNR/Cohn			10. SPONSORING/MONITORING AGENCY REPORT NUMBER DTRA-TR-01-21	
11. SUPPLEMENTARY NOTES This work was sponsored by the Defense Threat Reduction Agency under RDT&E RMC Code B 462D D E620 AB GE 25904D. 25904D.				
12a. DISTRIBUTION/AVAILABILITY STATEMENT Approved for public release; distribution is unlimited.			12b. DISTRIBUTION CODE	
13. ABSTRACT (Maximum 200 words) A technique to determine the radial distributions of the electron density and temperature in a plasma radiation source (PRS) from radially resolved spectra of optically thin dopants is described herein. A space and time resolved Johann spectrometer and a version with a modified high spectral resolution film circle were constructed for this purpose. The observed values for the temperature sensitive Ly _α and He _α plus intercombination (IC) line intensity ratio and the density sensitive IC/He _α line ratio is compared to calculated values to determine local values n _e and T _e . The density profile inferred this way from Si spectra observed on Double Eagle with Al wire loads coated with 5% Si have a minimum on-axis which increases with radius. The minimum on-axis is attributed to opacity effects whereas the larger value in the corona is attributed to He _α radiation emitted in the core that is absorbed and remitted (scattered) by He ions in the corona. A density profile that monotonically decreases from an on-axis maximum is deduced if this scattering of core radiation is included in this analysis. The calculated spectra are sufficiently sensitive to the assumed radial distributions to provide confidence in their uniqueness.				
14. SUBJECT TERMS Johann spectrometer Microchannel plates Ion temperature Imaging Spectrometer Intercombination line Z-pinch density			15. NUMBER OF PAGES 71	
17. SECURITY CLASSIFICATION OF REPORT UNCLASSIFIED			18. SECURITY CLASSIFICATION OF THIS PAGE UNCLASSIFIED	
19. SECURITY CLASSIFICATION OF ABSTRACT UNCLASSIFIED			20. LIMITATION OF ABSTRACT SAR	
16. PRICE CODE				

CONVERSION TABLE

Conversion Factors for U.S. Customary to metric (SI) units of measurement.

MULTIPLY \longrightarrow BY \longrightarrow TO GET
 TO GET \longleftarrow BY \longleftarrow DIVIDE

angstrom	1.000 000 x E -10	meters (m)
atmosphere (normal)	1.013 25 x E +2	kilo pascal (kPa)
bar	1.000 000 x E +2	kilo pascal (kPa)
barn	1.000 000 x E -28	meter ² (m ²)
British thermal unit (thermochemical)	1.054 350 x E +3	joule (J)
calorie (thermochemical)	4.184 000	joule (J)
cal (thermochemical/cm ²)	4.184 000 x E -2	mega joule/m ² (MJ/m ²)
curie	3.700 000 x E +1	*giga bacquerel (GBq)
degree (angle)	1.745 329 x E -2	radian (rad)
degree Fahrenheit	$t_K = (t_F + 459.67)/1.8$	degree kelvin (K)
electron volt	1.602 19 x E -19	joule (J)
erg	1.000 000 x E -7	joule (J)
erg/second	1.000 000 x E -7	watt (W)
foot	3.048 000 x E -1	meter (m)
foot-pound-force	1.355 818	joule (J)
gallon (U.S. liquid)	3.785 412 x E -3	meter ³ (m ³)
inch	2.540 000 x E -2	meter (m)
jerk	1.000 000 x E +9	joule (J)
joule/kilogram (J/kg) radiation dose absorbed	1.000 000	Gray (Gy)
kilotons	4.183	terajoules
kip (1000 lbf)	4.448 222 x E +3	newton (N)
kip/inch ² (ksi)	6.894 757 x E +3	kilo pascal (kPa)
ktap	1.000 000 x E +2	newton-second/m ² (N-s/m ²)
micron	1.000 000 x E -6	meter (m)
mil	2.540 000 x E -5	meter (m)
mile (international)	1.609 344 x E +3	meter (m)
ounce	2.834 952 x E -2	kilogram (kg)
pound-force (lbs avoirdupois)	4.448 222	newton (N)
pound-force inch	1.129 848 x E -1	newton-meter (N-m)
pound-force/inch	1.751 268 x E +2	newton/meter (N/m)
pound-force/foot ²	4.788 026 x E -2	kilo pascal (kPa)
pound-force/inch ² (psi)	6.894 757	kilo pascal (kPa)
pound-mass (lbm avoirdupois)	4.535 924 x E -1	kilogram (kg)
pound-mass-foot ² (moment of inertia)	4.214 011 x E -2	kilogram-meter ² (kg-m ²)
pound-mass/foot ³	1.601 846 x E +1	kilogram-meter ³ (kg-m ³)
rad (radiation dose absorbed)	1.000 000 x E -2	**Gray (Gy)
roentgen	2.579 760 x E -4	coulomb/kilogram (C/kg)
shake	1.000 000 x E -8	second (s)
slug	1.459 390 x E +1	kilogram (kg)
torr (mm Hg, 0° C)	1.333 22 x E -1	kilo pascal (kPa)

*The bacquerel (Bq) is the SI unit of radioactivity; 1 Bq = 1 event/s.

**The Gray (GY) is the SI unit of absorbed radiation.

Table of Contents

SECTION	PAGE
CONVERSION TABLE	ii
FIGURES	v
TABLES	vii
1. EXECUTIVE SUMMARY.....	1
2. INTRODUCTION.....	5
2.1 MOTIVATION	5
2.2 SPECTROMETERS	8
2.3 OVERVIEW OF PROGRAM	10
3. IMAGING HIGH RESOLUTION SPECTROMETERS.....	15
3.1 SPECTROMETER DESIGN CONSIDERATIONS	15
3.2 GEOMETRICAL OPTICS OF CRYSTAL SPECTROMETERS	16
3.3 GEOMETRICAL OPTICS DESIGN OF A HIGH RESOLUTION EXTENDED RANGE SPECTROMETER (HY-REX)	18
3.3.1 HY-REX Spectrometer	25
3.4 SPACE AND TIME RESOLVED JOHANN SPECTROMETER	26
3.4.1 Design Consideration	26
3.4.2 Space and Time Resolved Spectrometer	27
3.5 DETERMINATION OF THE INSTRUMENT SPECTRAL RESPONSE..	32
4. MEASUREMENT OF T_i , N_i , AND T_e WITH IMAGING SPECTROMETERS...	35
4.1 INTRODUCTION	35
4.2 ION TEMPERATURE MEASUREMENTS	35
4.2.1 T_i on Double Eagle	36
4.2.2 T_i on Saturn	38
4.2.3 T_i on DM-2 with Gas Puff Loads	40
4.2.4 Summary of Ion Temperature Measurements	42
4.3 RADIAL DISTRIBUTION OF ELECTRON DENSITY AND TEMPERATURE IN A Z-PINCH.....	44
4.3.1 Determination on $n_e(r)$ and $T_e(r)$ by Method 1	44
4.3.2 Determination of $n_i(r)$ and $T_e(r)$ Using the He_α or IC Intensity Profile	49
4.3.3 Alternate Approach to Inferring Radial Density and Temperature Profiles	50
4.3.4 Summary of Radial Density and Temperature Profile Measurements	54
 APPENDIX	
A. BIBLIOGRAPHY.....	A-1

Table of Contents (Continued)

Distribution List.....	DL-1
------------------------	------

Figures

Figure	Page
1 Dependence of $\text{He}_\alpha/\text{IC}$ intensity ration on electron density	7
2 Schematic of time and space resolved Johann spectrometer	11
3 Geometry for calculating x-ray trajectory	17
4 Best focus circle relative to Rowland circle for crystal at 45°	18
5 Best focus circle for a range of crystal angles	19
6 Schematic of HY-REX spectrometer incorporating best focus design	20
7 Figure of merit $\lambda/\Delta\lambda$ of HY-REX spectrometer for ADP crystal at 25°	22
8 Figure of merit $\lambda/\Delta\lambda$ of HY-REX spectrometer for ADP crystal at 45°	22
9 Figure of merit $\lambda/\Delta\lambda$ of HY-REX spectrometer for ADP crystal at 55°	23
10 Figure of merit $\lambda/\Delta\lambda$ for Johann geometry	23
11 Film cassette of HY-REX spectrometer	26
12 Instrument circle for maintaining Johann geometry when crystal is rotated	27
13 Assembly drawing of time and space resolved Johann spectrometer	28
14 Photograph of time and space resolved Johann spectrometer	29
15 Photograph of imaging slit mechanism	30
16 Cross section of plates used to focus imaging slits	31
17 Photograph of microchannel plate detector	32
18 Approximation of K_α lines by Gaussian distribution	33
19 Distribution of observed line widths obtained with electron beam excited K_α source	34
20 Al He_β and Si He_α lines on Double Eagle	37
21 Satellite Al He_α lines on Double Eagle	37
22 Mg He_α and IC lines on Saturn	38
23 Mg Ly_α on Saturn fit by two Gaussian functions	39
24 Uncertainty in Abel inversion routine associated with smoothing the data ..	40
25 Uncorrected radial distribution of ion temperature on DM-2	41
26 Micro densitometer scan of Cl He spectrum	42
27 Dependence of center line wavelengths of Cl He_α and IC lines on axial position	42
28 Radial distribution of Abel inverted line intensities	46
29 Two Gaussian fit to Al He_δ and Si Ly_α lines	46
30 Calculated contours of $\text{Ly}_\alpha / (\text{He}_\alpha + \text{IC})$ line ratio	47
31 Calculated contours of $\text{IC}/\text{He}_\alpha$ line ratio	47
32 Radial distribution of electron temperature and ion density inferred from $\text{IC}/\text{He}_\alpha$ and $\text{Ly}_\alpha / (\text{He}_\alpha + \text{IC})$ line ratio	48
33 Radial distribution of electron temperature and ion density inferred from IC intensity and $\text{Ly}/(\text{He}_\alpha + \text{IC})$ line ratio	50

Figures (Continued)

Figure		Page
34	Electron density profile inferred with and without photo excitation processes	52
35	Ratio of radiative to collisional excitation rates	53

Tables

Tables	Page
1 Relationship of cassette angle and crystal angle	21
2 Calculated values for $\lambda/\Delta\lambda$ of commonly used analyzing crystals	24
3 $\lambda/\Delta\lambda$ for x-ray detectors when $\theta=45^\circ$	24

Section 1

Executive Summary

The radiative properties of a z-pinch are determined by the ion temperature T_i , ion density n_i and electron temperature T_e achieved in the pinch. The time resolved values of n_i , T_i and T_e and their spatial distribution would provide valuable information about physical process occurring during the implosion and stagnation phases of the pinch which could be used to improve yield and spectral fidelity of the source.

Procedures used to-date have inferred the average electron densities and temperatures of z-pinchs by comparing both the measured intensity ratio of dominant spectral lines and the total radiation yield with calculated values obtained from collisional radiative equilibrium (CRE) model calculations. [1] Since optically thick lines have been used in these studies, the total line intensity, averaged over the pinch radius, have to be calculated for different assumed radial distributions of the electron density and temperature. The new feature of the work described herein is to use an imaging spectrometer to obtain the distribution of optically thin spectral lines perpendicular to the pinch axis. These line intensities can be Abel inverted to obtain their radial distributions, from which the local density and temperature can be inferred using the same CRE codes. The use of the density sensitive intercombination (IC) to He_α line ratio in this analysis is new to the z-pinch community. Trace amounts of optically thin dopants are used to minimize complications due to opacity and line intensity ratios used to eliminate the need for absolutely calibrated spectrometers or radiation yield measurements. The measured K-shell yield can now be used to bench mark the spectral analysis routine.

HY-Tech chose the Johann spectrometer for this study because it provides both the spectral range necessary to measure the line intensities of interest and sufficient spectral resolution to measure the Doppler width. The Doppler width is required to infer ion temperatures, which are used in the CRE calculations. The Johann geometry employs a concave cylindrical crystal to disperse and focus the radiation from an extended source

onto a detector circle, called the Rowland circle, thereby eliminating source broadening. HY-Tech has designed and constructed both time resolved and time integrating spectrometers in which the crystal and detector can be moved independently to maintain the Johann geometry as the crystal tilt angle is varied to continuously access different spectral ranges. The time resolved version employs four imaging slits and four gated striplines on the microchannel plate detector to record four time and space resolved spectra. The integrated version utilizes film recording in a modified configuration (HY-REX) where a best focus circle replaces the Rowland circle. In this version all x-rays reflected from the crystal are optimally focused, not only those from the center of the crystal, thereby extending the range of high spectral resolution. The spectral resolution of the HY-REX instrument was measured using an electron beam excited K_{α} source to have a figure of merit $\lambda/\Delta\lambda \sim 1850$ for ADP and KAP crystals used in first order. This limiting value is attributed to the mosaic structure of the crystals and may be much higher when used in higher order or with other crystals, such as Si (111).

The time resolved version included an alignment laser for pointing the spectrometer at the x-ray source and imaging slits which can be opened to facilitate imaging a bright light source at the pinch location onto the striplines of the detector. All four slits can be translated as a unit to accomplish this positioning and then closed down to the proper slit width for recording. A 40 mm x 45 mm microchannel plate detector with 6 mm wide striplines provides complete spatial imaging of the spectra at both ends of the detector with more spatial resolution than is currently available in any K-shell spectrometer. The film recording version features a shutterless film cassette design that utilizes a light tight Be window entrance aperture. With this cassette no data is lost because the shutter was inadvertently left closed.

The film version was fielded on a number of simulators to evaluate the design concept of maintaining the Johann geometry when the crystal was rotated and to evaluate the analysis routine for inferring the density and temperature distributions. Ion temperatures

were inferred from optically thin dopants (Mg or Si) in Al Alloy wire loads imploded on Saturn and Double Eagle in both the short (60 – 90 ns) and long (120 – 200 ns) current pulse modes. The ion temperature was in the range of 3 – 5 keV in the short pulse mode, where radiation pulse lengths were 29 – 43 ns compared to 7 – 9 keV in the long pulse mode where a large number of wires were used and the radiation pulse was shorter (8.4 to 19 ns). Since the electron temperatures are consistently inferred to be in the 1 – 1.5 keV range these results indicate that the lower value of T_i/T_e and hence greater degree of thermalization, are obtained with the shorter current pulse. Since the radiation pulse was longer in this case, the degree of thermalization appears to be determined by the radiation pulse length and not the current pulse length.

The first radial ion temperature distribution was obtained on the DM-2 generator at Maxwell PI imploding an Ar gas puff load. A monotonic distribution was observed which decreased from an uncorrected value of 9 – 10 keV on-axis to 5 keV at a radial position of 3.5 mm. These values are in the range observed with wire loads in the long pulse mode. Axially resolved x-ray spectra were obtained which exhibited a spatially varying center line wavelength whose variation appears to be larger at the cathode end of the pinch. Doppler velocities inferred from these wavelength shifts are about one-half the implosion velocity anticipated when the η parameter is approximately 1. Their origin, though not understood, reveals new information about implosion dynamics.

The analysis routine for inferring the radial distribution of the electron density and temperature from the radial distributions of the $Ly_\alpha/(He_\alpha + IC)$ and IC/He_α line ratios was evaluated using Si spectra obtained on Double Eagle with Si coated (5%) Al wire loads. The analysis predicted a density distribution with an on-axis minimum which increased radially. The on-axis depression was not a surprise since the optical depth is estimated to be 1.6 at the center of the pinch. However, the density was expected to decrease when r exceeded some value r_0 where opacity was no longer an issue. The erroneous increase in density that was inferred for $r > r_0$ was shown to be due to a scattering process proposed by

Apruzese et al. [2] where intense He_α radiation from the core of the pinch is absorbed and reemitted (scattered) by He ions in the low density outer region of the pinch. The very large difference between the photo excitation rates of the He_α line and the IC line (a factor of 230) results in a reduced IC/ He_α line ratio which is characteristic of a large electron density if this scattering processes is not taken into account. The analysis by Apruzese et al. [2] has shown that the CRE model can be used to model the observed intensity distribution. In this case, the spatially resolved intensity of an x-ray line emergent from the pinch is calculated at different perpendicular distances from the pinch axis while taking into account photo excitation by radiation from the core. The predicted spectrum is sufficiently sensitive to the assumed density and temperature distribution that this procedure can be used to infer these distributions with a high degree of confidence in their uniqueness.

The time resolved spectrometer was not fielded on any simulators to determine its relative virtues.

Section 2

Introduction

2.1 Motivation

The radiation characteristics of a z-pinch plasma radiation source (PRS) are affected by the plasma density and temperature achieved in the pinch, their spatial distribution, the stability of the pinch, and the thermalization of the implosion kinetic energy. Knowledge of these plasma parameters provides information about the physical processes occurring during the implosion and stagnation phases of the pinch. The ion temperature can be an indication of the implosion velocity acquired by the imploding ion and the resulting opacity of the plasma. Axial and radial inhomogeneities may be a measure of magneto-hydrodynamic instabilities in the plasma whereas the ratio of the electron and ion temperatures and non-thermal electron energies are a measure of thermalization and micro instabilities occurring during the stagnation phase. A comparison of the measured values of these parameters with theoretically calculated ones is required to benchmark codes used to predict scaling relationships in larger radiation sources. A more critical evaluation of these codes is possible if they are subject to the more stringent requirements of predicting the radial plasma distribution in the pinched plasma as well as the x-ray yield and pulse length.

The intensity of spectral lines emitted by a plasma can be related to the internal plasma conditions using collisional radiative models which incorporate these plasma processes. An iterative procedure has been employed where the various line intensity ratios and total radiative yield are calculated for assumed plasma conditions and compared with observed values. [1] This procedure is repeated until convergence is achieved. This procedure can be significantly simplified if optically thin lines are studied since radiation transport does not need to be included in the analysis. The procedure is further simplified if the radially resolved intensity distribution of the emitted lines are available to infer the radial distribution of plasma parameters. The program described herein is concerned with

combining spectroscopic techniques with one-dimensional imaging to obtain either the radial or axial distributions of plasma parameters. Optically thin dopants are used to obtain these parameters with minimal complications due to opacity and line intensity ratios are used to eliminate the need for absolutely calibrated radiation yield measurements. These yield measurements, along with the $Ly_{\alpha}/He_{\alpha} + IC$ line ratio, are required by the procedure used in reference [1] to determine the average electron density and temperature. The measured K-shell yield can now be used to bench mark the spectral analysis routine.

The intensity of spectral lines depends, in general, on both the ion density and electron temperature. The ratio of intensities from different ionization states is particularly sensitive to the electron temperature. The ratio of the Lyman alpha (Ly_{α}) to the $He_{\alpha} +$ Intercombination (IC) intensities has been used extensively for this purpose. [1] Calculations have shown that the ratio of the He_{α} and Li like jkl dielectronic satellite lines is also proportional to the electron temperature and relatively insensitive to the electron density and can be used for this purpose. [3] The IC line, on the other hand, is collisionally excited and is therefore particularly sensitive to the electron density. Its ratio with the He_{α} line is relatively independent of the electron temperature for T_e greater than some critical, $T_c(z)$, which increases with atomic number as shown in Figure 1 which is taken from Ref [4]. These three line ratios are the candidates for inferring the radial electron density and temperature profiles in the pinch. Only the intensity, integrated over the ion line profile, must be Abel inverted for each spectral line being analyzed.

Different electron density and temperature regimes can be probed by incorporating trace amounts of higher atomic number materials into the load material as the temperature and densities increase. Practical limitations of this technique exist since it is not always possible to obtain loads with the desired trace elements. It is straightforward to include F, Ne, O, N, Cl, or Ar as optically thin trace elements in gas puff loads. However, there are plasma temperature/density regimes where an element between Ne and Cl is desirable,

such as Si, which is only available as a toxic gas. Similar problems are encountered with wire loads where alloys of Al containing S or P are not available.

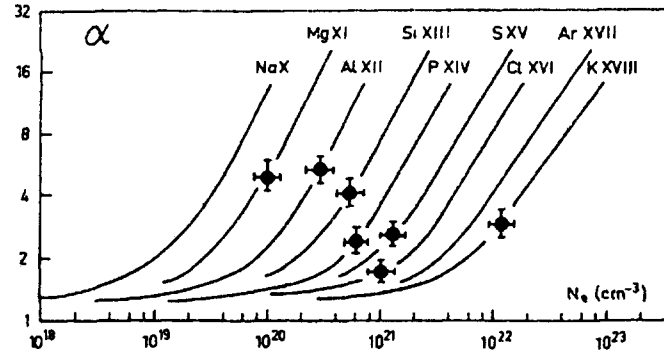


Figure 1. The Ne dependence of the $\text{He}_\alpha/\text{IC}$ intensity ratio for several He-like ions. The calculations were made at the following electron temperature values: Na9+, Te = 250 eV; Mg10+, 340 eV; Al11+, 360 eV; Si12+, 420 eV; P13+, 490 eV. S 14+, 560 eV; Cl15+, 710 eV; Ar16+, 760 eV; and K17+, 800 eV. Experimental values are shown by dots with error bars. [4]

There are more fundamental problems associated with relating the IC/ He_α line ratio to electron density if the plasma contains non-thermal electron beams. In this case, the radiation may be polarized, and if the spectrometer is polarization sensitive, the intensity ratio may be different for polarization parallel or perpendicular to the electron beam and beam effects must be included in the analysis of the line intensities. [5] Although this complicates the analysis, it also provides a diagnostic tool to probe the electron density distribution, which can significantly affect the radiation characteristics of PRS's.

The Stark broadening of hydrogen and helium like lines is an analysis technique for inferring the electron density that does not depend on line intensities. This technique has been used extensively to determine plasma densities in magnetic confinement devices [6] and it has recently been extended to laser-produced plasmas and z-pinches. [7,8] The densities inferred in this way can be compared with those inferred from line ratios for self-consistency. Unlike ratio measurements, where only the intensity of the line must be Abel inverted for radially resolved density measurements, the Stark technique requires the spectral line profile to be Abel inverted, wavelength by wavelength, for this purpose. This can introduce some error into the measurement. Furthermore, the Doppler

broadening must be deconvoluted from the total line profile to determine the Stark contribution, which is usually significantly less than the Doppler contribution. Any residual opacity broadening further complicates the analysis process making this technique difficult, but not impossible to apply.

In addition to plasma density distribution measurements, spectroscopic techniques can be used to infer the ion temperature profile from the Doppler width of optically thin lines. As in the case of Stark broadening, the measured intensity must be Abel inverted to obtain the radially resolved line profile from which the radial ion-temperature profile can be inferred. These ion temperature measurements are required for the CRE calculations.

2.2 Spectrometers

High resolution spatially imaging spectrometers are required to infer the plasma parameters described above. Spectrometers employing convex, flat and concave crystals have been used to record x-ray spectra in the range of 0.7 to 15 keV. Low dispersion convex crystals are used in survey spectrometers to record the entire spectrum emitted by the source. These spectrometers have limited energy resolution since monochromatic x-rays emitted from different locations in the source are recorded at different locations at the detector. This source broadened energy resolution is inadequate to resolve the Doppler width of the line and to resolve the He_{α} , IC and Li like satellite lines in some cases, and is not considered for this program.

Cylindrical, spherical and elliptical crystal spectrometers have been employed to overcome source broadening by focusing monochromatic x-rays onto one point at the detector. [9] The Johann geometry employing a cylindrical crystal of radius, R , is one of the simplest and widely used varieties. [10] The rays are focused onto a cylindrical surface known as the Rowland circle. A slit parallel to the dispersion plane images the plasma perpendicular to the dispersion direction. Only a limited length of the crystal satisfies the Bragg criteria which limits the numerical aperture (NA) or brightness of the

spectrometer. The NA can be increased by using an elliptical crystal to focus radiation from a source located at one focus of the ellipse onto the detector located at the other focus. [9] The elliptical crystal spectrometer has found numerous applications for studying laser produced plasmas. [3]

The Johann geometry was chosen for this program because it has a larger spectral range than the other focusing varieties and the required crystals are easier to obtain. However, the Johann spectrometer has limitations which must be addressed if high spectral resolution is desired over a broader spectral range. Trajectory calculations indicate that only those rays of energy, E_0 which are reflected where the Rowland circle is tangent to the crystal are focussed onto it. Rays with energy $E < E_0$ focus behind the Rowland circle and rays with $E > E_0$ focus in front of it. These trajectory calculations can be used to define a best focus circle where all of the x-rays from an extended source, that are Bragg reflected from the entire length of the crystal, are optimally focused. The "best focus" circle defined in this fashion replaces the Rowland circle in a modified Johann geometry which extends the energy range over which high spectral resolution measurements are possible. A kinematic mount has been designed which preserves the best focus geometry when the detector and crystal are rotated to access different spectral ranges. The spectral advantage achieved with the best focus detector and film recording is lost when a flat microchannel plate detector is utilized in a time-resolved spectrometer.

Any spectrometer that uses a slit to image the source in one dimension (say the radial direction), averages the radiation over the other dimension (i.e. along the pinch length). Axially averaging the transverse displacements of a kink-like distribution results in a broader radial distribution and transverse velocities in the pinch become averaged to a broadened Doppler profile. Some aperturing is required to observe only one axial position in the pinch if localized measurements are desired. Wong et al. [11] claimed that the required localization could be obtained by placing an aperture on an "imaging circle" which they defined as a circle with radius $R/4$ tangent at the crystal surface. HY-Tech's

ray-tracing code indicates this is not the case since polychromatic rays emitted from one point in the pinch do not pass through one point on the “imaging circle” as claimed in Ref. 11 or any surface near by. An aperture placed here would affect the energy spectrum recorded. We have shown that a film placed near the crystal or far beyond the Rowland circle can be used to obtain a 2-D image of the pinch in the wavelength of each line emitted by the pinch. An aperture placed at this location will select an axial position for that wavelength. Separate apertures are required for each wavelength probed.

2.3 Overview of Program

Three spectrometers were modified or constructed in the course of this work. First, a survey spectrometer was converted to a Johann version which included a film cassette mounted on an arm connected to the crystal mounting stage. This arrangement preserved the Johann geometry while the crystal was rotated to access different spectral ranges. Next, a high resolution extended range (HY-REX) spectrometer was designed and constructed which incorporated the best focus circle concept. The Bragg angle can be varied from 18° to 55° to access a large spectral range with a given crystal. The film is precisely located using a positive locking mechanism to press it against the curved “best focus” contour. A shutterless light-tight configuration is achieved using a pinhole free 12.5 mm thick Be foil entrance window that is transparent to the x-rays of interest. With this configuration scintillation from the crystal is excluded from entering the cassette. The cassette can be transported without special precautions and spectra are not missed because the operator forgot to open the shutter.

The last design utilizes four (4) entrance slits together with four (4) gated striplines on a microchannel plate detector to record time resolved spectra from the pinch. A schematic representation of this spectrometer showing three (3) of the 4 slits employed is presented in Figure 2. A square microchannel plate detector with 6 mm wide striplines is employed to cover the full spectral range of the crystal at every time probed. A sliding vacuum seal allows the spectrometer body, on which the detector is mounted, to rotate relative to the

crystal and thereby maintain the Johann geometry when the latter is rotated to access a different spectral range. The spectrometer includes a number of features which facilitate the alignment of the instrument. This includes an alignment laser that can be introduced through a side port, for rough alignment. Fine tuning the alignment is achieved using the slit assembly, which can be translated to position the image on the center of the microchannel plate detector striplines. The widths of the slits can be increased for

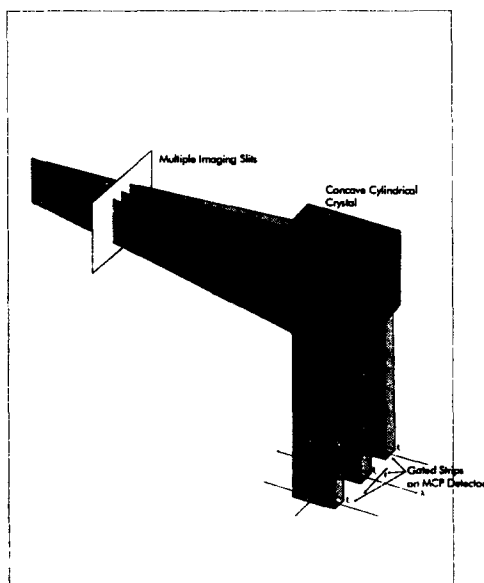


Figure 2. Multiple slits (three in this case) are used to produce three spectra which are spatially resolved in the direction perpendicular to the slits and dispersion plane of the crystal. Three spectra are imaged onto three striplines of a microchannel plate detector which is gated to record three spatially resolved spectra at times t_1 , t_2 and t_3 in the emission pulse. Radially resolved but axially averaged intensities distributions of each spectral line are recorded if the slits are aligned with the pinch. Viewing an alignment light source at the pinch location and then precisely adjusted to optimize the x-ray intensity.

viewing an alignment light source at the pinch location and then precisely adjusted to optimize the x-ray intensity.

Measurements of the spectral resolution of these instruments using a cold electron beam source reveals a figure-of-merit $\lambda/\Delta\lambda$ about 1850. This value is a factor of 3 less than the theoretical value for an ADP crystal (6000) and orders of magnitude less than the

calculated value for the geometrical optics design of the HY-REX spectrometer. The mosaic properties of the crystal appear to determine the resolution of the spectrometer in the spectral range of 5–9 Å.

The spectrometers were used to study the characteristics of pinched plasmas on the DM-2 and Double Eagle accelerators at Maxwell Physics International and on Saturn at Sandia National Laboratories in both the short (60 – 100 ns) and long (120 – 200 ns) current pulse modes. The measurements reveal ion temperatures in range of 3 – 5 keV on both Saturn and Double Eagle from Al wire loads in the short pulse modes. The measured values are larger in the long pulse mode (6.9 ± 1.4 keV on Saturn and $8.5 \pm .8$ keV on Double Eagle). These HY-Tech values are considerably smaller than the 5-45 keV values inferred by Sanford et al. [12] from time resolved spectral measurements on Saturn in the short pulse mode. The latter ion temperatures were inferred from survey spectra by taking into account source broadening and the effects of opacity. The significance of this discrepancy to the simulator program lies in the current understanding of radiation processes in the pinch. Attempts to model the observed spectrum and x-ray yield from the pinch cannot be simultaneously reconciled with the lower ion temperature measured by HY-Tech. If this discrepancy is more than the difference between time resolved and time averaged spectra, then these measurements can be indicative of the different degrees of thermalization that have been achieved. A lesser degree of thermalization would be expected in Sanford's case where a large number of wires (90) led to a shorter radiation pulse (3-5 ns) than the 25 ns pulse achieved with 24 wires in case of shot 2396 studied by HY-Tech. If, on the other hand, the resolution of Sanford's spectrometer is insufficient to measure a lower temperature value, the difficulty with reconciling the measured yield with theoretical calculations deserves more study.

HY-Tech has sought direct evidence for non-thermal electron beams by analyzing the first and second order spectra obtained with two orthogonally oriented spectrometers on Saturn. Results to date have not shown any polarization properties that would be

indicative of e-beams. The absence of polarized x-rays may not be evidence for thermal plasma. The null result may be due to depolarization by the optically thick plasma and/or the reduced polarization (by 40%) that is expected when viewing the pinch at 55° to its axis.

The radial distribution of the electron density and temperature were inferred from the x-ray spectra using three different approaches. The first two approaches related the Abel inverted intensities of measured spectral lines to values calculated by J. Apruzese [13] for a uniform plasma column having the same pinch diameter using a collisional radiative equilibrium (CRE) model. In both cases the $Ly_\alpha/He_\alpha + IC$ line ratio of a 5% Si dopant was used together with either the IC/He_α line ratio or the IC intensity to infer local values for the electron density and temperature. The density profile inferred from the IC/He_α approach exhibited an on-axis depression due to opacity effects and radially increasing density which has been attributed to the absorption and reemission (scattering) of radiation from the interior of the plasma column by the coronal plasma. [2] Since the scattering cross section is 230 larger for the resonance He_α line than the IC line, the value of IC/He_α is depressed implying a larger electron density. The second approach used the intensity profile of the He_α line, instead of the IC/He_α ratio in an attempt to avoid these opacity and scattering effects. Since the spectrometer was not absolutely calibrated, the calculated intensity at some radial position r_0 was used to normalize the intensity profile at all other radial positions. The intensity at r_0 was calculated using the density and temperature inferred from the IC/He_α approach. The value of r_0 was chosen midway between the regions where the opacity and scattering are expected to dominate. Although a realistic density profile was obtained which decreased monotonically from a peak on-axis, no criterion can be identified for selecting r_0 . These attempts led to the third method which is described in detail in Ref [2]. In this case, the radial intensity profiles of the lines prior to Abel inversion were modeled by calculating the line integrated intensity emergent along a line perpendicular to the pinch axis. The spatially dependent scattering was included in the calculations. An iterative procedure was used in which the radial

density and temperature profile were varied to obtain the optimal fit with the spectral line profiles. The spectral profiles were sufficiently sensitive to the assumed density and temperature distributions to indicate that a unique distribution was identified. These results clearly established that radial electron density and temperature profiles in the radiating pinch can be inferred from radially resolved spectral measurements.

The remainder of the report is organized as follows. The next section describes the design, fabrication, and testing of the spectrometer used in this study. This is followed by a section describing the ion temperatures, ion density distributions and electron temperature distributions studied in this program.

Section 3

Imaging High Resolution Spectrometers

3.1 Spectrometer Design Considerations

The spectral resolution of a x-ray spectrometer depends on the dispersion and focusing properties of the optical design and the resolving power of the crystal employed. The geometrical optics design provided the only avenue for improvement since the resolving power of the crystal and the resolution of detector systems are fixed quantities.

Numerous spectrometer designs have evolved which provide different levels of collection efficiency, spectral resolution, and compensation for source broadening. In general, the spectral range sampled with a given detector diminishes as the spectral resolution increases. Density determination from Stark broadening favors a higher spectral resolution instrument whereas a wider spectral view is required if the density is inferred from the ratio of a few spectral lines. The decision to infer densities from line-ratio measurements favored the simple Johann geometry for this application.

A Bragg crystal spectrometer in the Johann geometry [10] employs a cylindrical concave crystal with radius r_c to disperse the x-rays in the plane of curvature. Monochromatic x-rays, emitted from an extended source, are Bragg reflected from this crystal and focused onto a detector surface known as the Rowland circle, thereby eliminating source broadening of the spectral line. The Rowland circle, with radius $r_c/2$, is tangent to the center of the crystal. The spectral range sampled depends on the $2d$ spacing of the crystal employed, the grazing angle the incident x-ray makes with the crystal surface, the length of the crystal, and the spectral range subtended by the detector. Different spectral ranges can be sampled by changing the crystal or rotating both the detector and crystal as a rigid body about an axis through the point of tangency between the Rowland circle and crystal surface.

The spectral resolution that is obtained with this instrument depends on the geometrical optics design of the crystal/detector geometry, the dispersion and mosaic properties of the crystal, and the dimensions of the detector medium. The highest spectral resolution is obtained with photographic film which can be bent to lie on the Rowland circle. Kodak type 2497 has the smallest grain size, 0.8 μm , but is significantly less sensitive than Kodak direct exposure film having a grain size of 1.8 μm . Time resolved measurements can be made with a gated microchannel plate detector. The spectral resolution in this case is significantly less than with film because the minimum resolvable dimension is approximately 60 μm and the detector is flat, which can contact the curved Rowland circle at no more than 2 points.

3.2 Geometrical Optics of Crystal Spectrometers

The focusing properties of the spectrometer were studied using a ray-tracing code that calculates the trajectory of x-ray photons emitted from different points in the pinch and Bragg reflected from a concave crystal of radius, r_c . This model can be used to determine the dispersion relation for the spectrometer as well as evaluate and optimize the focusing properties of the crystal. The code is based on the trigonometric expression for the dispersion of the spectrometer which relates the distance, Z , along the detector of radius, r_f , to the photon energy, E , the crystal 2-d spacing, and the emission site location, s , on the source. The source, crystal, and detector circle geometry are shown in Figure 3. The dispersion relation is given by $Z = \alpha r_f$ where subject to the Bragg relation.

$$\alpha = 2\theta + \delta - \sin^{-1}\left(\frac{b}{r_f} \sin[\pi - (2\theta + \delta)]\right) \quad (1)$$

$$b = r_c \sin \theta - x + \frac{r_c \cos \theta - y}{\tan(2\theta + \delta)} \quad (2)$$

$$\delta = \frac{r_c \cos \theta - s}{h + r_c \sin \theta} \quad (3)$$

$$\sin(\theta + \delta) = \frac{n\lambda}{2d} = \frac{n12.39}{2dE(keV)} \quad (4)$$

Here x, y are the coordinates of the detector center, whose radius is r_f , relative to the crystal center $(0,0)$, h is the source to spectrometer distance, r_c is the crystal radius, and n is the spectral order. The geometrical energy resolution of the spectrometer is given by the expressions

$$\Delta E = \frac{dE}{dZ} \Delta Z \quad (5)$$

$$\Delta Z = Z_+(E) - Z_-(E) \quad (6)$$

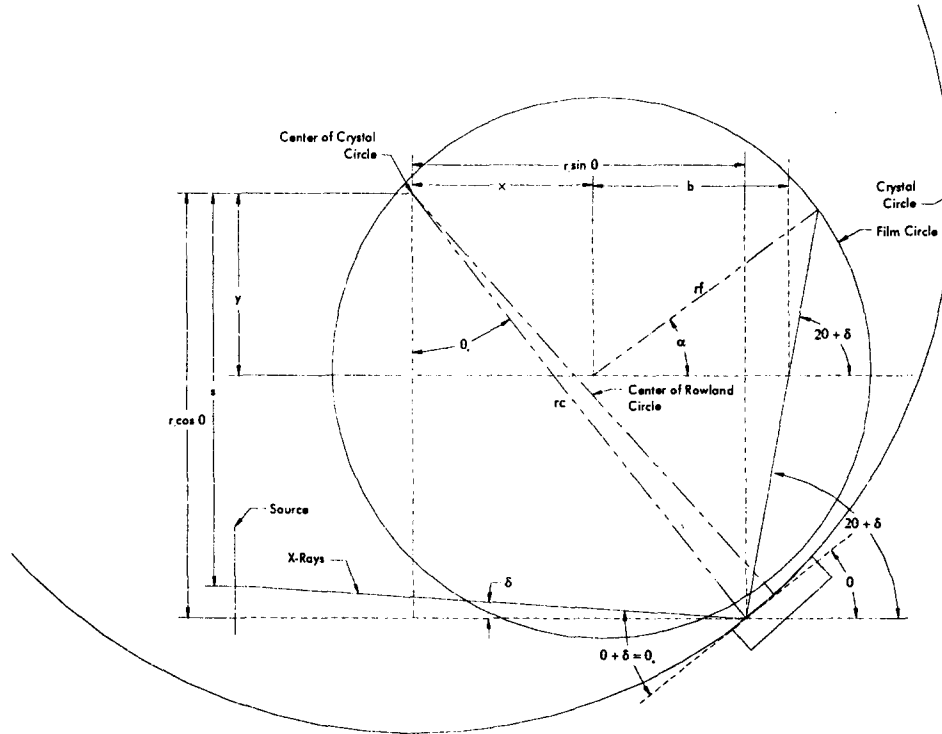


Figure 3. Geometry for calculating trajectory of x-rays Bragg reflected from concave crystal of radius r_c . Origin of coordinates is at center of crystal circle. The angle θ_0 corresponding to the middle of the crystal is referred to as the crystal tilt angle in text. The film circle radius $r_f = r_c/2$ in the Johann geometry with its origin at the midpoint of the crystal radius at angle θ_0 . The Bragg angle is $\theta_B = \theta_0 + \delta$ with $Z = \alpha r_f$, the distance on the film between a spectral line and a horizontal reference line.

Here, ΔZ is the length of an extended source observed on the detector surface which is determined by the focusing properties of the cylindrical surface. $Z_{\pm}(E)$ are calculated for monochromatic rays emitted from the two ends of the source.

3.3 Geometrical Optics Design of a High Resolution Extended Range Spectrometer (HY-REX)

The capability of the Johann geometry to correct for source broadening was studied by calculating the trajectory of monochromatic x-rays emitted from two locations on the source. This was repeated for energies reflected from the center of the crystal and the two ends. Rays with energy E_0 reflected from the center, where the Rowland circle is tangent to the crystal, are focused onto it. Rays with $E > E_0$ are focused in front of the Rowland circle while those with $E < E_0$ behind it. This can be seen in Figure 4.

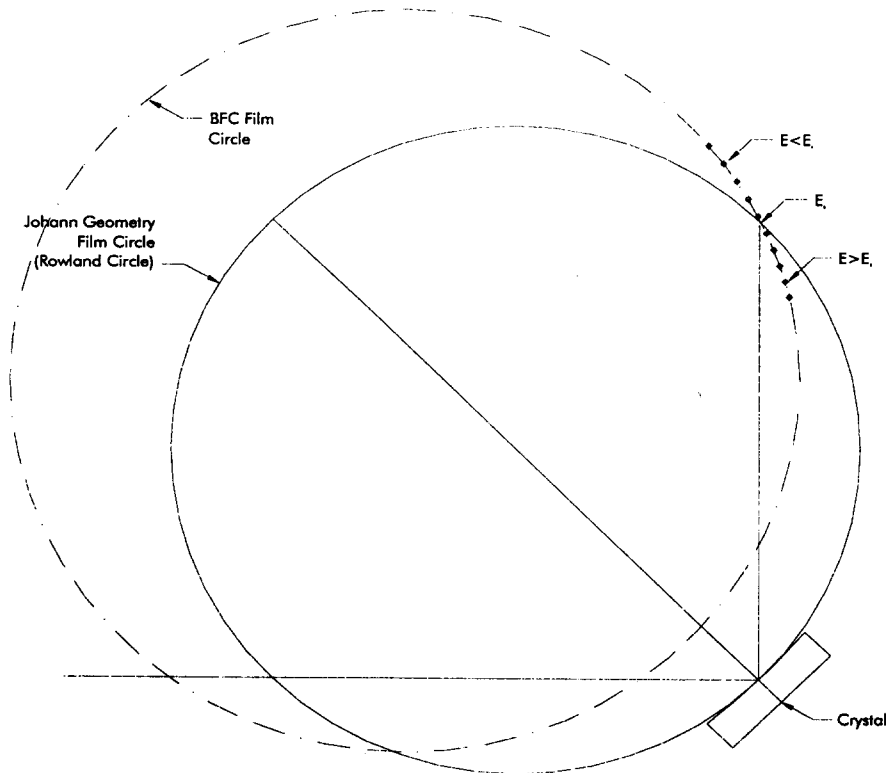


Figure 4. The loci of all x-ray energies focused by the crystal are shown on a best focus circle for a crystal tilt angle $\theta_0 = 45^\circ$. Rays with energy $E > E_0$ are focused in front of the Rowland circle and those with $E < E_0$ behind it.

The optimal focusing surface was sought using an expanded ray-tracing model which followed the trajectories of 10 rays emitted from equally spaced location on the source. The size of the spot formed by the rays crossing an image plane perpendicular to the central ray was calculated as the image plane was stepped along the ray until a minimum was found. This was repeated for all energies reflected from the crystal. A curve through these focus points could be approximated by a "best focus circle" that does not coincide with the Rowland circle. This is shown in Figure 4 for a crystal tilt angle $\theta = 45^\circ$. The calculations were repeated for different crystal tilt angles from $20^\circ - 60^\circ$ and the appropriate "best focus circle" identified in each case. These circles are shown in Figure 5. The data points on the best-focus-circles are the loci of all x-ray energies that are

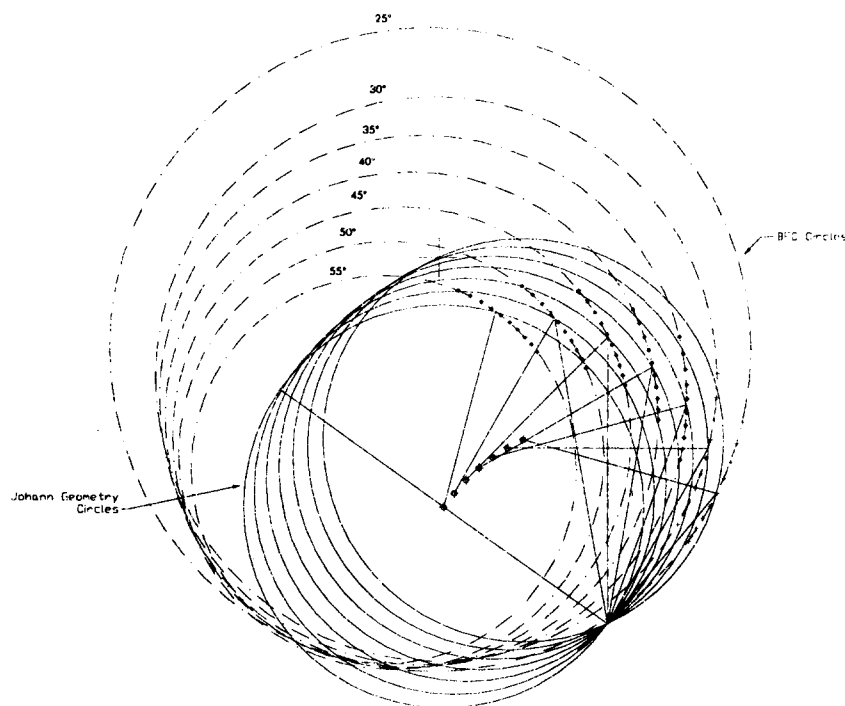


Figure 5. Best focus circles and Rowland circles for a range of crystal tilt angles. The BFC crosses the Rowland circles where the rays reflected from the crystal center are found.

Bragg reflected from the 5 cm long crystal. The radius of these curves varied between 11.88 and 19.48 cm. The detection portion of the best focus circle from $\theta = 45^\circ$ was found to closely approximate the detection region of the other best focus circles if it was rotated, together with the crystal, using the two (2) arm mechanism shown in Figure 6.

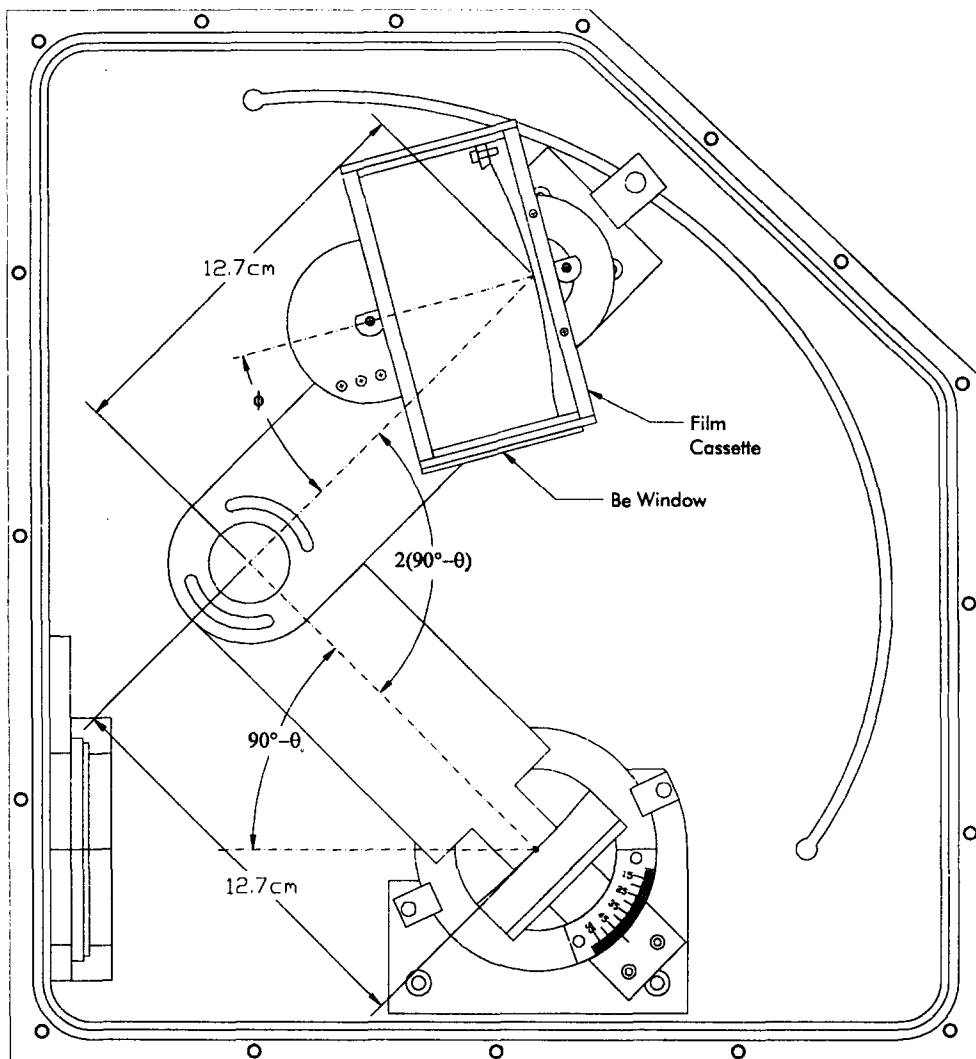


Figure 6. Two arm rotation scheme used in the HY-REX spectrometer to position the film surface on the best focus circle as the crystal tilt angle θ_0 is varied. The angle Φ must be set for different ranges of the angle θ_0 as given in Table I. The dial sets the angle θ_0 and locator pins set the angle Φ in 5 steps. A 12.5 μm Be window forms a light tight shutterless window for the film cassette which is clamped to the spectrometer body by a dog that slides in the curved groove.

The crystal and film cassette are mounted at the ends of two arms whose other ends are jointly pivoted. The crystal can rotate about an axis tangent to its front face to set the angle θ_0 defined in Figure 3. This angle is approximately the Bragg angle at the center of the crystal. Setting the angle between the two arms at $2(90^\circ - \theta_0)$ positions the center of the film cassette on the Rowland circle. The angle, Φ , between the normal to the film surface and the second arm must also be set at an angle θ_0 for the film surface to coincide with

the best focus circle. Representative values of Φ for the accessible range of θ_0 are presented in Table I. The calculated geometrical optics properties of a 25 cm radius

Table 1. Relationship of cassette angle Φ in Figure 6 to the crystal angle θ_0 .

Crystal angle θ_0	Cassette angle Φ
15	7.497
20	9.836
25	12.102
30	14.217
35	17.158
40	17.808
45	19.116
50	19.948
55	20.15

crystal 5 cm long are presented next. In this case, the lengths of arms A and B are both 12.7 cm, and the film cassette radius is 18.39 cm. These values are determined by the geometry of the spectrometer and should scale with the crystal radius. The range of Bragg angles that are accessible for each crystal angle is approximately $\theta_0 \pm 3.8^\circ$. The figure-of-merit, $\lambda/\Delta\lambda$, for this best focus geometry have been calculated for 10 equally spaced energies reflected from the crystal. The results are presented for the best focus geometry for crystal tilt angles of 20° , 45° , and 55° in Figures 7 - 9. Similarly, results are presented in Figure 10 for a crystal tilt of 45° in a Johann geometry. The large values for $\lambda/\Delta\lambda$ that is predicted for the full range of tilt angles presented in Figures 7 - 9 demonstrates the feasibility of using the rotation mechanism in Figure 6 to approximate the best focus geometry. The extended range of enhanced spectral resolution achievable with the best focus design relative to the conventional Johann geometry is clearly evident from these figures-of-merit calculations.

The focusing property of the crystal will also contribute to the instrumental width of the spectrometer. Values for $\lambda/\Delta\lambda$ have been calculated for commonly used crystal analyzers. [14] Some representative values have been presented in Table 2.

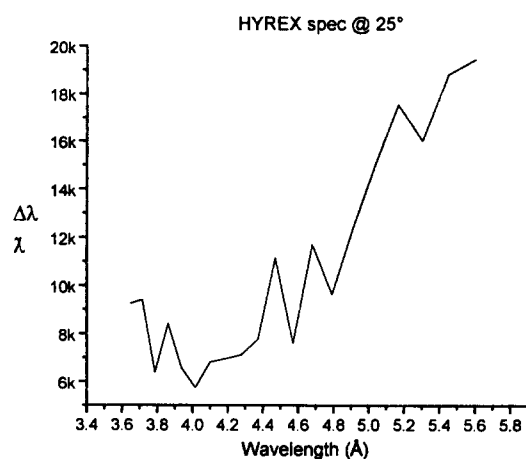


Figure 7. Dependence of the figure of merit, $\lambda/\Delta\lambda$, on the wavelength for the HY-REX spectrometer with an ADP crystal ($2d=10.6 \text{ \AA}$) at a tilt angle of 25° .

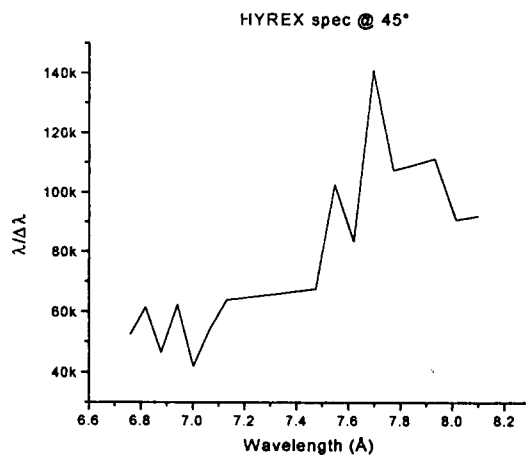


Figure 8. Dependence of the figure of merit, $\lambda/\Delta\lambda$, on the wavelength for the HY-REX spectrometer with an ADP crystal ($2d=10.6 \text{ \AA}$) at a tilt angle of 45° .

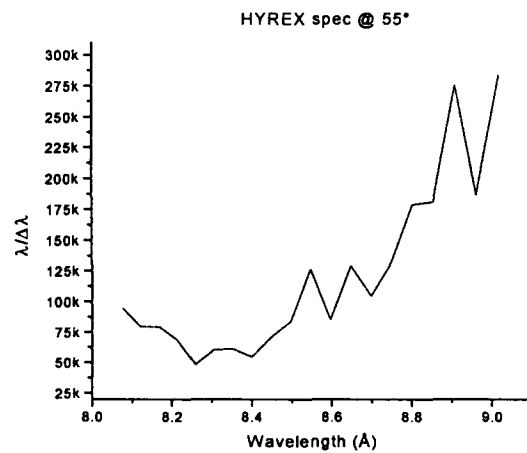


Figure 9. Dependence of the figure of merit, $\lambda/\Delta\lambda$, on the wavelength for the HY-REX spectrometer with an ADP crystal ($2d=10.6 \text{ \AA}$) at a tilt angle of 55° .

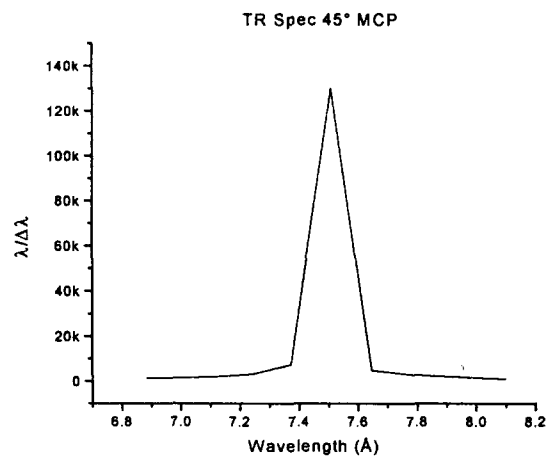


Figure 10. Dependence of the figure of merit, $\lambda/\Delta\lambda$, on the wavelength for the Johann geometry with an ADP crystal ($2d=10.6 \text{ \AA}$) at a tilt angle of 25° .

Table 2. Calculated values of $\lambda/\Delta\lambda$ for crystals commonly used in PRS studies.
Values taken from Ref [14].

		1 st Order			
Line	Wavelength (Å)	KAP (001)	MICA (002)	ADP (101)	Si (111)
Al K α	8.153	1930	3440	6680	
Ti K α	2.746	2250	3580	6300	7700
Cu K α	1.5398			6350	7010
		2 nd Order			
Al K α	8.153	13,900	12,100		
Ti K α	2.746	29,000	13,100		
Cu K α	1.5398	42,500	14,600		

The crystal appears to limit the resolution in the best focus design case where as the geometrical optics limits the resolution in the Johann configuration for wavelength 0.1 Å from the center wavelength.

The contribution of the recording medium to the instrument function is given by the product of the spectrometer dispersion, $d\lambda/dZ$, and the minimum resolvable spectral feature, ΔZ_d of the detector. Values for $\lambda/\Delta\lambda$ are presented in Table III when the crystal tilt angle is 45° for grain sizes and pixel dimensions commonly encountered in x-ray spectroscopy.

Table 3. $\lambda/\Delta\lambda$ for x-ray detectors when $\theta = 45^\circ$

Defector	ΔZ_d	$\lambda/\Delta\lambda$
DEF Film	1.3 μm	199,000
2497 Film	.8 μm	323,000
Microchannel Plate	60 μm	4,300

An approximation for the instrument function of the spectrometer can be obtained by assuming that the geometrical optics design, crystal resolving power, and detector resolution can be approximated by Gaussian distributions whose full widths at half

maximum (FWHM) are given by $\Delta\lambda_g$, $\Delta\lambda_c$, and $\Delta\lambda_d$, respectively. Then the instrument function is given by a Gaussian whose FWHM is given by the expression

$$\Delta\lambda_i = \left(\Delta\lambda_g^2 + \Delta\lambda_c^2 + \Delta\lambda_d^2 \right)^{1/2} \quad (7)$$

It is clear that only film recording can take advantage of the high spectral resolution that the best focus design has to offer. These design features were incorporated into the HY-REX film recording spectrometer described below.

3.3.1 HY-REX Spectrometer

The assembly drawing for the HY-REX spectrometer is presented in Figure 6. The crystal angle θ_0 is set using the dial shown. The angle between the arms linking the crystal and film cassette is set using templates while the tilt angle, Φ , of the cassette can be varied in five (5) equal steps using set-pins.

The film cassette consists of a base plate, a film clamp and a cover. An exploded view of the base plate and "U" shaped clamp is presented in Figure 11. A single angled stop locates the low energy end of the film as shown at the top of the cassette in Figure 6. Two short angled stops are used at the high-energy entrance end of the cassette to locate the outside edges of the film without obstructing grazing angle x-rays entering the cassette. This feature allows measurements to be made at Bragg angles as shallow as 13° . A precisely cut piece of film is inserted sideways under these angled stops to locate the film. The edges of the "U" shaped clamp are contoured to clamp the film securely to the best-focus-circle contour of the base plate. A 12.5 mm Be foil on the cover forms a light tight entrance aperture to the cassette. The film cassette is precisely positioned on its support arm by two locating pins. The cassette is evacuated when the system is pumped down through light tight vacuum ports. This "shutterless" concept allows the cassette to be carried to and from the dark room with minimal precautions and avoids lost data, which results when a mechanical shutter is not opened. Kimfoil filters at the entrance port of the spectrometer protect the crystal from pinch debris.

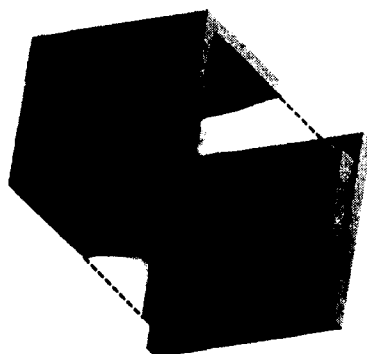


Figure 11. Exploded view of film cassette showing “U” shaped clamp which presses the film against the base plate.

3.4 Space and Time Resolved Johann Spectrometer

3.4.1 Design Consideration

The Johann geometry was chosen for this application to provide optimal source broadening compensation for the central wavelength consistent with the limited spectral resolution of the gated microchannel plate detector. The locus of points where the rays, Bragg reflected from the center of the crystal, intercepts the best focus circles can be fitted by a circle of radius 28.65 cm for $25^\circ \leq \theta \leq 55^\circ$. The center of the circle, called the instrument circle, is shown in Figure 12. It is the trajectory on which the center of the detector must move when the crystal is tilted to access different spectral ranges. The detector will be approximately tangent to the Rowland circle if the detector is set at an angle of 17.6° to the tangent of the instrument circle in Figure 12.

The figure-of-merit for the geometrical optics design of this space-time spectrometer is approximately the same as that of the Johann shown in Figure 10 even though it has a flat detector. This geometrical limitation must be combined with the spectral limitations imposed by the pixel size of the gated microchannel plate detector in Table III and the

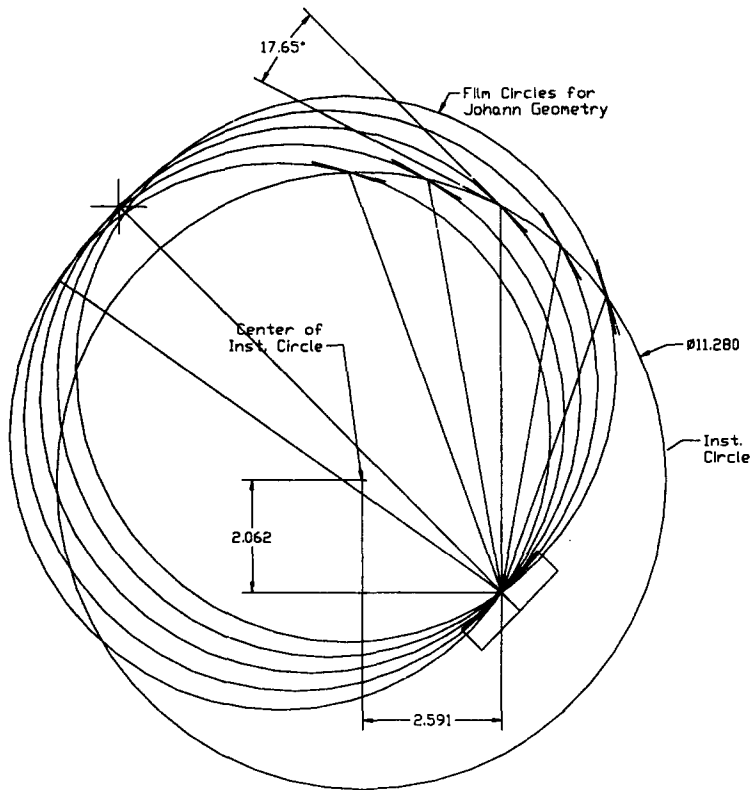


Figure 12. Instrument circle on which detector is rotated to maintain Johann geometry as crystal tilt angle is varied from 35° to 55° . The coordinates of the crystal rotation axis, relative to the center of the instrument circle, are given in inches for a crystal radius of 25.4 cm (10 inches).

crystal in Table II to obtain an estimate of the spectral resolution of the instrument.

3.4.2 Space and Time Resolved Spectrometer

A space and time resolved Johann spectrometer was constructed which incorporated the design considerations described above. This four frame unit combines four input slits with four gated striplines on the microchannel plate to obtain spatially resolved spectra at four times during the x-ray emission pulse. A three-slit version of the design concept is

shown in Figure 2. Special features incorporated in the design included a square detector with 6 mm wide strips to provide full spectral coverage at each time interval with good spectral resolution. Other bells and whistles include a diode laser whose machined housing automatically aligns the beam axis with the spectrometer axis when inserted into the instrument. This laser aims the spectrometer at the source before the slits are in place. The input slits, whose width can be adjusted while maintaining parallel alignment of the edges, can be opened with a micrometer drive to image a bright light at the source location onto the microchannel plates for fine alignment purposes. The slits can be translated to center the image on the microchannel stripline and then closed down to the proper width for data acquisition. A tip tilt stage aligns the system with the source.

An assembly drawing of the spectrometer system is shown in Figure 13 and a photograph of the fabricated instrument is shown in Figure 14. The spectrometer

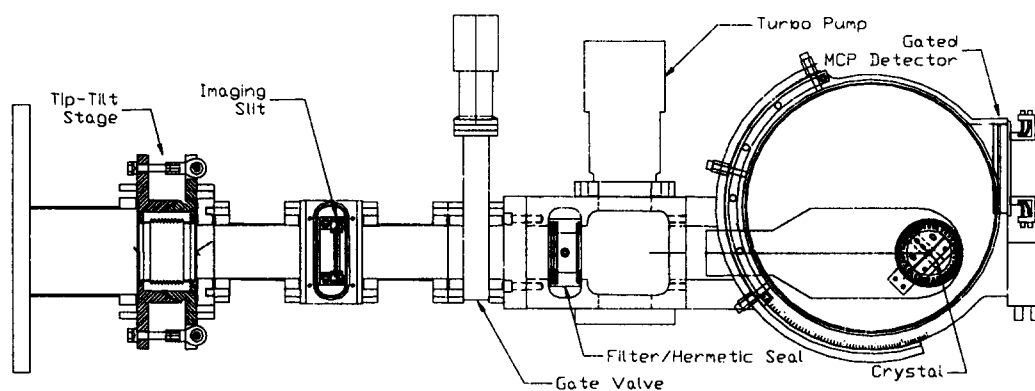


Figure 13. Assembly drawing of the time resolved imaging Johann spectrometer. The round spectrometer body is rotated to position the detector and maintain the Johann geometry when the crystal is rotated to accesses different spectral ranges.

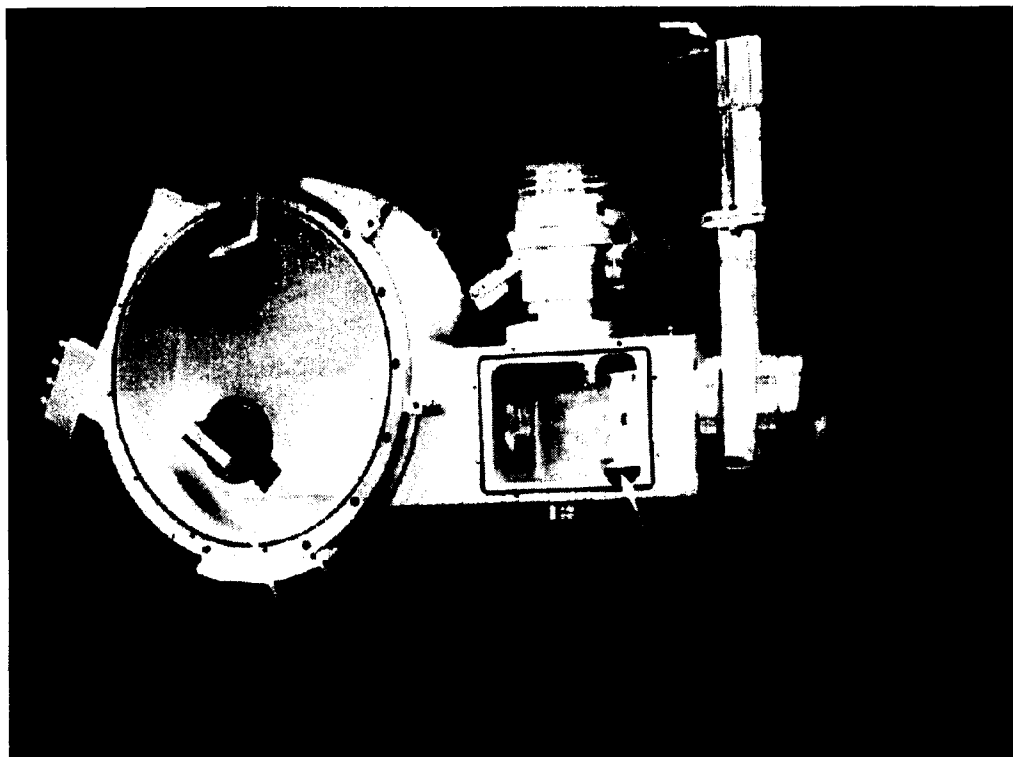


Figure 14. Photograph of the time and space resolved spectrometer with cover plates removed to expose the crystal and microchannel plate detector. The three screw clamps, on one side of the spectrometer, which draw the round rotating section to the rigid half round shell are seen as well as two from the other side.

system is connected to the simulation chamber via a tip/tilt stage at the left of the figure for aligning the instrument with the source. The imaging slits are contained in a separate housing between the chamber and the spectrometer. The lengths of the vacuum tubes connecting this component are chosen to provide the proper magnification. A pneumatically operated gate valve isolates the spectrometer from the simulation chamber when the latter is up to air. This is followed by a rectangular filter housing on which a turbo-molecular pump is mounted. The crystal is mounted on a rotary stage which is supported by a paddle-shaped plate affixed to the filter box as shown in Figures 13 and 14. The round spectrometer body is connected to the filter section via a sliding vacuum seal which allows the former to be rotated relative to the latter. A scribed scale on the spectrometer body is designed to position the center of the detector at the location where the crystal focuses the x-rays whose Bragg angle is θ_0 . A dial sets the crystal angle with a precision of 6 min and the scribed scale on the rotating portion of the housing positions the detector with an accuracy of $1/4^\circ$.

An 8.3 μm Kapton filter, located at the end of the filter box in Figure 14, hermetically isolates the spectrometer from the remainder of the system. This seal allows the spectrometer body to be evacuated by the turbo pump to the proper pressure (3×10^{-6} Torr) required by the microchannel plate detector. A 12.5 μm Be foil will be used to filter out the uv radiation produced by the pinch. A by-pass line connects the volume between the gate valve and hermetically sealed Kapton filter to the spectrometer chamber. A pneumatically operated valve in this line is automatically opened when the gate valve is closed and the main chamber is up to air to equilibrate the pressure across the hermetic seal. This valve is closed when the gate valve is opened for data acquisition. The 4 entrance slits used to produce the 1-dimensional images of the spectra on the 4 microchannel plate strip lines are shown in Figure 15. One micrometer is used to translate the slits relative to the housing for positioning the image on the detector strips while the other one is used to adjust the slit widths. The slit width is adjusted by translating a plate

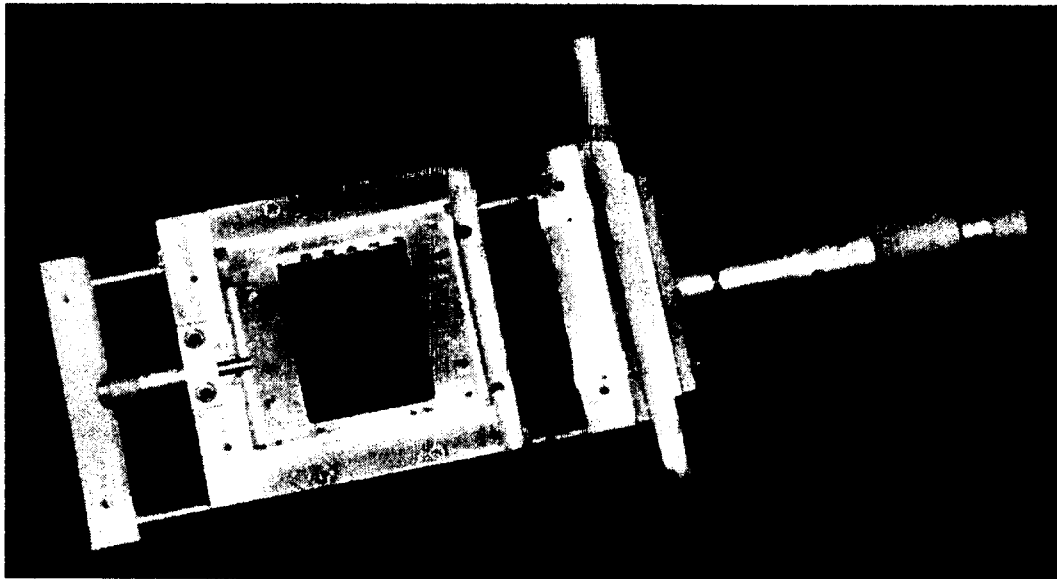


Figure 15. Photograph of the 4 imaging slit mechanism. Micrometer on left translate the upper plate relative to the lower plate to change the width of the slits the while micrometer on right translates the slits to image the pinch on to the microchannel plate striplines.



Figure 16. The four imaging slits are formed by two plates having machined angled slots. Traslating the upper plate with the micrometer on the left side of Figure 15 realtive to the lower one varies the width of the slits.

having 4 slots, 0.6 mm wide, relative to a similar plate to vary the over lap of the slots. The slots were cut by an electrical discharge machine with 15° sloping walls, as shown in Figure 16, to provide a sharp knife-edge for the slits. The slits are parallel to within 15 μm over their 4.4 cm length.

The microchannel plate detector is shown in Figure 17. Gold is evaporated onto 6 mm wide strips to form a photoelectron-emitting surface. The strips have an impedance of 12.5 Ω and are fed by a four (4) parallel 50 Ω coaxial cables. The edge of the vacuum housing for the detector has been specially designed to be flush with the surface of the microchannel plate. X-rays at grazing angles of incidence as low as 10° can be detected with this geometry.

A high voltage pulse generator and fan-out box are used to generate four pulses that gate the microchannel striplines. The on-time is determined by the pulse length and the temporal separation between the pulses is set with cables having the desired delay length.



Figure 17. The 6 mm wide Au photo emitting striplines on the 40x45 mm microchannel plate detector are shown along with the fingers making the connection with the two parallel coaxial lines providing the gate pulse.

3.5 Determination of the Instrument Spectral Response

The instrumental widths of the Johann and HY-REX spectrometers were inferred from measurements of K_{α} lines excited by a 10 keV electron beam incident on Al and Si targets. The tip of an Al wire was used as a target for producing a point source of x-rays while large bulk targets were used to mimic an extended source. Measurements were made at crystal tilt angles corresponding to Bragg reflections from each end of the crystal as well as the center to see if the predicted degradation in spectral resolution of the Johann geometry can be observed. The separation of the two K_{α} lines of Al and Si are 2.4 and 2.5 mÅ and their FWHM are 2.7 and 2.1 mÅ, respectively. [15] The spectral distribution of the source $g(\lambda)$ can be modeled by the sum of two Gaussian functions whose relative amplitude are in a ratio of 0.5. [16] The result is shown in Figure 18. Also

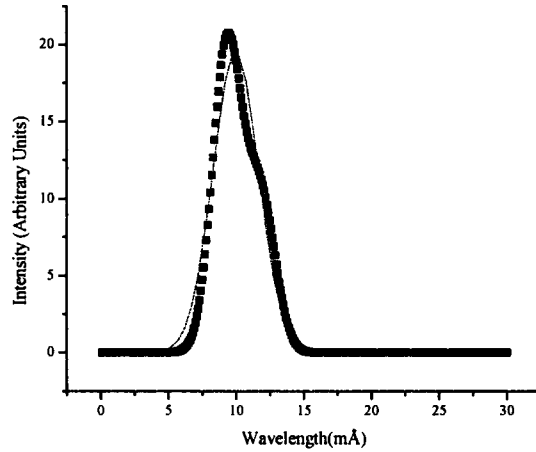


Figure 18. Approximation of the $K_{\alpha 1}$ and $K_{\alpha 2}$ lines of Al or Si spectrum excited with a 10 keV electron beam, by a Gaussian function whose width is $\Delta\lambda_s = 4$ mÅ.

shown is the fit to $g(\lambda)$ that is obtained with a Gaussian distribution having a FWHM $\Delta\lambda_s = 4$ mÅ. An estimate for the spectral resolution of the instrument can be obtained by assuming the instrument function $f(\lambda)$ can be approximated by a Gaussian whose FWHM is $\Delta\lambda_I$. A value for $\Delta\lambda_I$ can be inferred from the expression

$$\Delta\lambda_I = (\Delta\lambda_{OBS}^2 - \Delta\lambda_s^2)^{1/2} \quad (8)$$

where $\Delta\lambda_{OBS}$ is the FWHM of the observed line profile. The values for $\Delta\lambda_I$, inferred in this fashion, are presented in Figure 19. The scatter in the values for $\Delta\lambda_{OBS}$ limit the accuracy that can be obtained with these measurements, thereby justifying the approximation of the source function by a Gaussian.

The distribution of instrumental widths obtained with the ADP crystal is quite broad. Since errors tend to broaden a measured line width, the points distributed around the smaller values of $\lambda/\Delta\lambda_I$ can be averaged to give a realistic value for instrumental width. The average value for $\Delta\lambda_I$ is $\lambda/1850$ in this case.

The value of 1850 for $\lambda/\Delta\lambda$ inferred from these measurements is less than the calculated values for the geometrical designs presented in Figures 7 - 10, the crystal characteristics presented in Table II and the detector limitation in Table III. The crystals maybe the

limiting factor since the calculated values do not take in to account the broadening that is expected when the crystals are bent. A higher resolution crystal, such as Mica in third

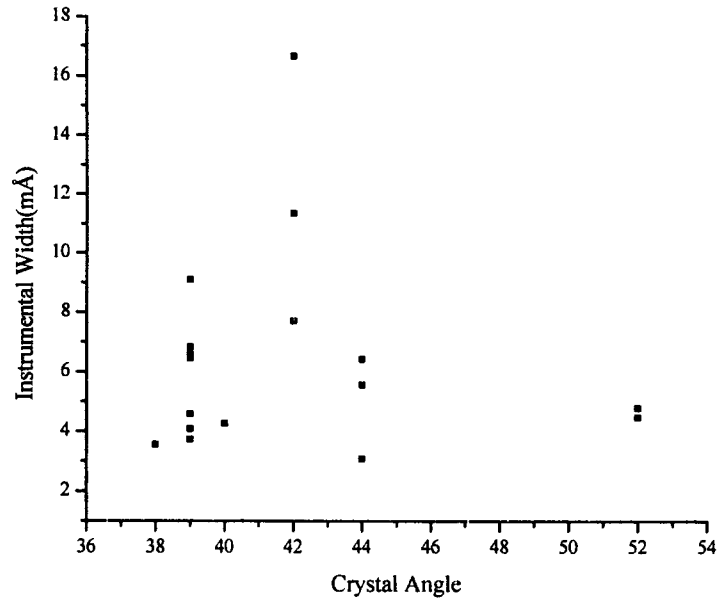


Figure 19. Distribution of instrumental widths inferred from measurements made at different crystal tilt angles using a electron beam excited K_{α} source.

order, could be used to further investigate this situation. The present results indicate that the Johann, HY-REX and time resolved Johann spectrometer can be characterized by an instrumental width $\Delta\lambda_i = \lambda/1850$ when KAP and ADP crystals are used in first order. There values may not be appropriate for the measurements made with the KAP crystal in 2nd order or with the Si (111) crystal in 1st order.

Section 4

Measurement of T_i , n_i , and T_e with Imaging Spectrometers

4.1 Introduction

The Johann and modified Johann (HY-REX) spectrometers constructed under this program were used to measure the radial and axial distributions of the ion line spectra emitted by z-pinchs. These spectra were analyzed to infer the distribution of ion temperatures, electron densities, and electron temperatures to demonstrate the practicality of using an imaging spectrometer to study these plasma parameters. Measurements were made on Double Eagle and Saturn with Al wire array loads in both the short and long current modes. Here, short refers to a current pulse that rises to maximum amplitudes in 60 ns on Saturn and 90 ns on Double Eagle. These current durations increased to 120 ns on Saturn and 200 ns on Double Eagle in the long pulse modes. Measurements were also conducted on DM-2, having a current pulse length of 300 ns, with Ar gas puff loads. These studies provide some insight into the different degree of thermalization achieved in the long and short pulse mode and possibly the difference between gas puff and wire load implosions. An analysis procedure has been developed, based on CRE calculations of the emitted line profiles, which can be used to infer the radial distributions of electron density and temperature with a high degree of confidence in their uniqueness.

4.2 Ion Temperature Measurements

The ion temperature is inferred from the Doppler width of the spectrally resolved profile of an ion line, which is optically thin. The spectral profile of the line emitted by the source can be inferred from the measured line profile by deconvoluting the contribution of the instrument response function. This can be most easily accomplished by assuming that both the observed line profile and the instrumental response function can be adequately approximated by Gaussian functions having FWHM of $\Delta\lambda_{\text{OBS}}$ and $\Delta\lambda_i$, respectively as described in Section 3.5. In this approximation, the source width $\Delta\lambda_s$ can be inferred using Equation (7) with the instrumental width $\Delta\lambda_i$ given by the value $\lambda/1850$

inferred in that section for KAP and ADP crystals. Unfortunately, $\Delta\lambda_i$ was not measured for KAP in 2nd order or for Si (111) crystals used in some of these studies.

In addition to Doppler broadening, the ion line profile can be broadened by Stark and opacity effects. The importance of Stark broadening increases for lines originating in higher Rydberg states and is absent from the IC lines considered in this study. These IC lines are essentially free of opacity broadening leaving them ideal candidates for inferring ion temperatures from their Doppler broadened line width with T_i given by the expression

$$T_i(\text{keV}) = 1.687 \times 10^5 \mu (\Delta\lambda_s/\lambda)^2 \quad (9)$$

where $\Delta\lambda_s$ is the full width at half maximum.

4.2.1 T_i on Double Eagle

In the short pulse mode, a current rising to 3.5 MA in 90 ns was used to implode an Al wire array coated with 5% Si. The spectrum around the Si IC line, shown in Figure 20, was recorded with a Johann spectrometer using a KAP crystal in second order. The spectral resolution is adequate to resolve the Al He_β and Si He_α lines which are separated by 12.7 mÅ with the entire spectrum adequately fitted by nine (9) Gaussian functions. The resonance lines and the Li like jkl satellites are identified in the figure. The observed width of the Si IC line was 6.9 mÅ which yielded a value for $T_i = 5$ keV if no corrections are made for the instrumental width of the spectrometer. It is not clear that the instrumental width $\Delta\lambda_i = \lambda/1850$, that was inferred in Section 3.5 for ADP and KAP crystals is applicable here since the theoretical spectral resolution of the KAP crystal in second order is a factor of 5 larger than its 1st order value. [14]

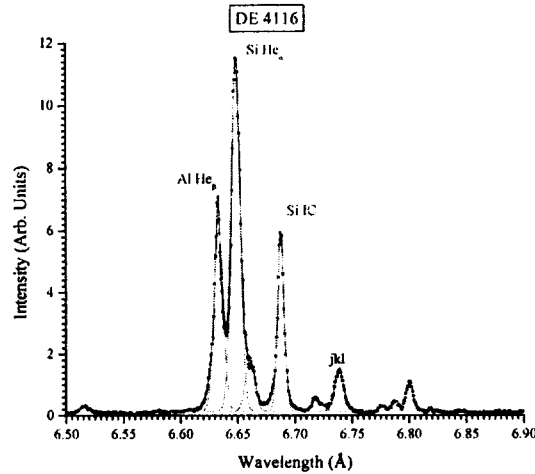


Figure 20. Gaussian fit to Al He $_{\beta}$ and the Si He like ion lines along with their associated dielectronic satellite lines. Spectra recorded with Al wire loads coated with 5% Si.

Al alloy wire loads containing 6% Mg were imploded by a 4.1 MA flat topped current pulse having a duration of 200 ns in the long pulse mode. The uncorrected ion temperatures that were inferred from fitting Gaussian functions to the measured profiles of the Mg Ly $_{\alpha}$, Al IC and Al jkl satellite line are 15.0, 11.9 and 9.5 keV, respectively. The spectra were recorded with a KAP crystal in second order and the fit to the satellite lines is shown in Figure 21. The ion temperature inferred from the satellite lines is expected to be the most reliable since it should exhibit the least amount of opacity

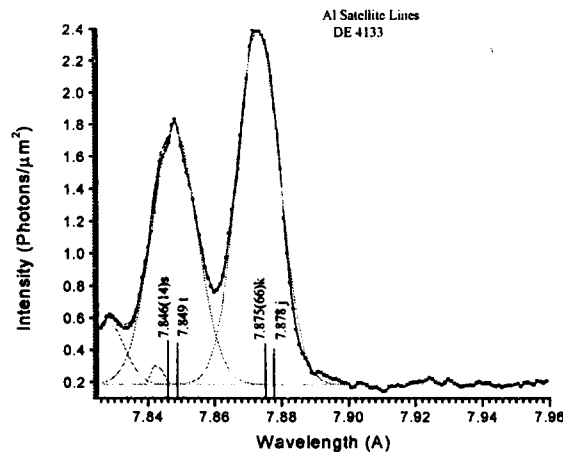


Figure 21. Gaussian fits to dielectronic satellite lines of He like Al ions. Wavelengths and relative amplitudes (in parenthesis) are from Ref. [17]

broadening. The larger width of the Mg Ly $_{\alpha}$ line may not be due to opacity effects, since this line is a P $_{3/2}$, P $_{1/2}$ hydrogen doublet having a separation of 6 mÅ. This is addressed in the next section.

4.2.2 T $_i$ on Saturn

Twenty-four (24) Al alloy wires containing 1% Mg were imploded on Saturn by a 8 MA current pulse rising to peak current in 60 ns. The Mg He like lines were recorded with an ADP crystal in first order. These are shown in Figure 22. The separation of the resonance and intercombination lines of Mg were calculated to be 3 mm on the Rowland circle using a ray-tracing code. This corresponded exactly to the separation of the two lines observed in the figure, which then were identified as shown. The half width of the Mg He $_{\alpha}$ line obtained with this dispersion is 8.7 mÅ, which corresponds to an uncorrected ion temperature of 3.7 keV and a corrected value of 2.7 keV.

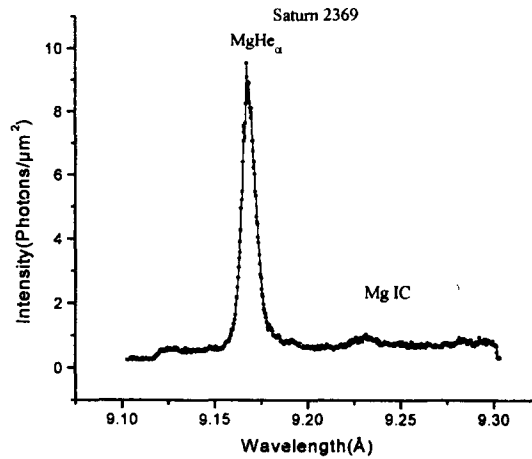


Figure 22. Mg He $_{\alpha}$ and IC lines obtained on Saturn with Al wire loads containing 1% Mg.

The ion temperature in the long pulse mode on Saturn were inferred from the spectra produced when a 280 Al wire array load containing 1% Mg was imploded by an 8 MA current pulse having a 140 ns duration. The uncorrected width of the Mg He $_{\alpha}$ line is 12.4 mÅ which corresponds to an uncorrected ion temperature of 7.5 keV and a corrected value of 6.3 keV. The corresponding values inferred from the uncorrected Mg Ly $_{\alpha}$ line

are 14.5 mÅ for the width and 12.2 keV for T_i . Since the Ly_α should be as optically thin as the He_α line, the Ly_α line profile was fitted by the sum of two Gaussian functions to see if the width can be attributed to the fine structure splitting of the hydrogenic line. The fitting was performed by constraining the individual Gaussians to have the same width but allowing all the other parameters to vary. The result is shown in Figure 23. The separation between the two fitted peaks is 7.9 mÅ which agrees very closely with the theoretical separation of 8 mÅ. The inferred intensity ratio is 0.54 which corresponds to calculated values for the $P_{3/2}/P_{1/2}$ intensity ratio when the plasma density $\sim 4 \times 10^{20} / \text{cm}^3$. [4] This latter value is consistent with ion density inferred from spectra obtained on Saturn. [13] The uncorrected ion temperature that is inferred from the width of the individual fine structure components is 6.9 keV which is very close to the 7.5 keV value inferred from the He_α line width. This analysis explains the large widths that have been observed from the Ly_α lines relative to the widths of other lines (He_α or satellite lines) on both Saturn and Double Eagle.

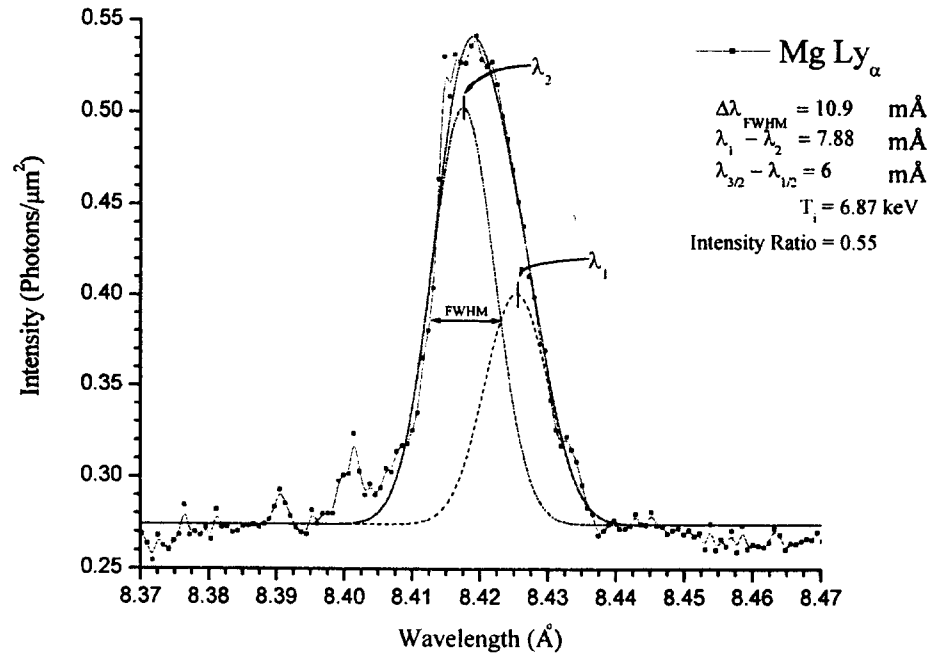


Figure 23. Fit to Mg Ly_α line by sum of two Gaussians representing fine structure splitting of hydrogenic line. Concentration of Mg was 1% in the Al wire load.

4.2.3 T_i on DM-2 with Gas Puff Loads

The radial profile of the ion temperature was measured on the DM-2 accelerator at Maxwell Physics International. The 2.1 MA current pulse having a duration of 285 ns, implodes a 7 cm diameter Ar gas puff load seeded with 4% Cl in 340 ns. The radial distribution of the ion temperature was obtained as follows. First the radial distribution of the ion line profile was divided into 56 equal wavelength intervals. The radial intensity distribution of each wavelength interval was then smoothed and Abel inverted. One such wavelength interval is shown in Figure 24 along with the uncertainty associated with the difference between the measured intensity and the smoothed value. The full width at half maximum is then determined at each radial position by fitting the line profile with a Gaussian. The resulting radial distribution of the uncorrected ion temperature inferred from the width of the IC line of Cl is shown in Figure 25.

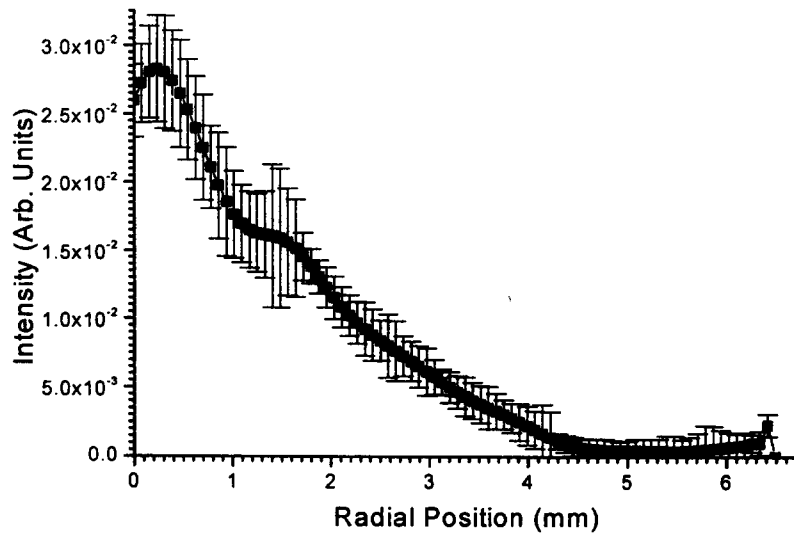


Figure 24. Abel inversion of radially smoothed intensity profile in one wavelength interval of the radially resolved IC line of Cl. Solid points represent smoothed values and error bars uncertainty between smoothed and actual values.

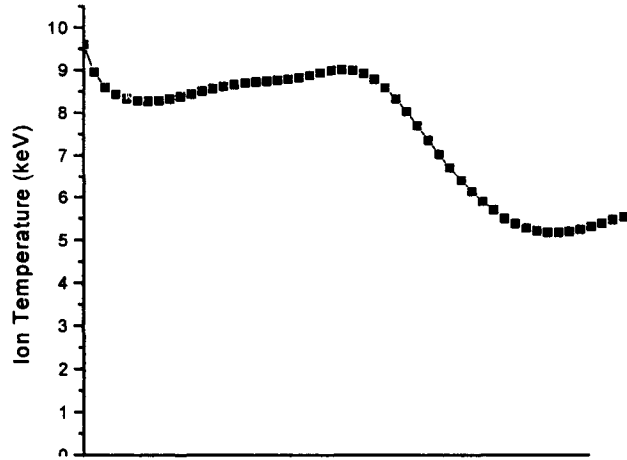


Figure 25. Uncorrected radial distribution of the ion temperature obtained from radially resolved Doppler widths of the IC line of Cl.

The axial variation of the ion line width was also studied. A very interesting feature that has been revealed by these measurements is the variation of the centerline wavelength with axial position as shown in Figure 26. The center line wavelength was determined for the He_α and IC lines at various axial positions and the results presented in Figure 27. The same trend in the wavelengths observed here for two closely spaced lines was also observed on the Ly_α and He_α line of Ar recorded with another spectrometer which indicates that this is not an instrumental effect. If these wavelength shifts are attributed to Doppler shifts due to motion of the pinch, we infer a peak-to-peak transverse velocity of $16 \text{ cm}/\mu\text{s}$ which is about one half the implosion velocity for an $\eta = 1$ plasma. [13] The origin of the Doppler shifts, if that's what they are, is unknown. However, the results provide additional information about the dynamics of the pinched plasma.

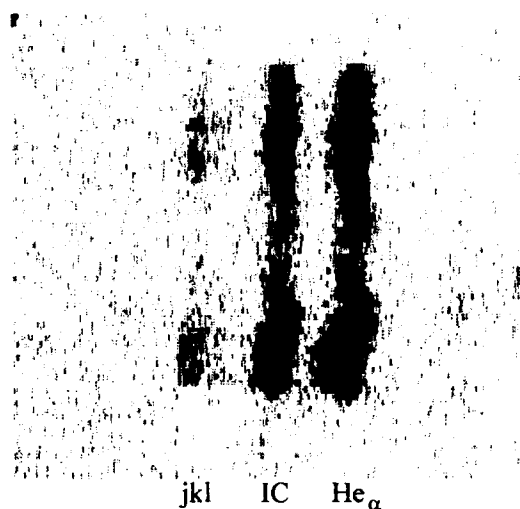


Figure 26. Micro densitometer scan of a Cl spectrum obtained with an axially resolved Johann spectrometer on DM-2. The anode is at the top of the figure and the cathode at the bottom.

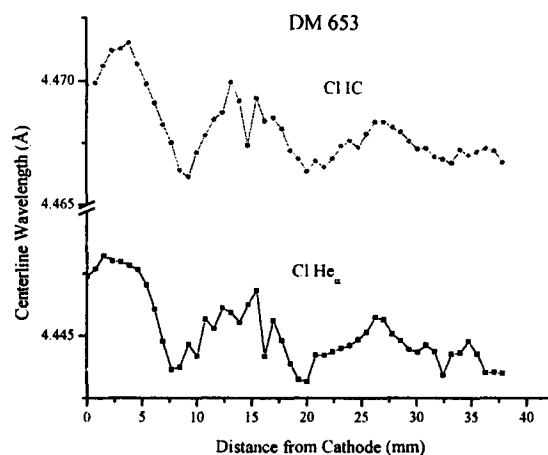


Figure 27. Axial distribution of the centerline wavelengths of the IC (upper) and He_α (lower) lines of Cl shown in Figure 26.

4.2.4 Summary of Ion Temperature Measurements

The uncorrected ion temperatures, inferred from optically thin lines, appears to be in the range of 3-5 keV for Al wire loads on both Saturn and Double Eagle in the short pulse mode. Larger values of 7.5 to 9.5 keV, respectively, were observed on these generators in the long pulse mode. A similar value (12.4 keV) was observed with gas puff loads on

DM-2 in the long current pulse mode. Since the electron temperature is consistently found to be in the range of 1-1.5 keV, the ratio, T_i/T_e is smaller in the short pulse mode. This ratio, which tends to 1 in a thermalized plasma, is a measure of how well the radiating pinch has thermalized. The larger values for this ratio in the long pulse mode may not be related to the current pulse length as much as it is to the radiation pulse length, since the latter maybe a measure of the time available for thermalization. The radiation pulse width in the short pulse mode was 43 ns on DE and 29 ns on Saturn. These pulse lengths decreased to 10-24 ns on DE and 9-20 ns on Saturn in the long pulse mode.

Another example linking a short radiation pulse to large T_i/T_e ratio was recently reported by Sanford et al. [12] They observed the ion temperature to temporally vary between 15 and 45 keV during the 5 ns radiation pulse when an array of 90 Al wires was imploded on Saturn in the short current pulse mode. Sanford's values for T_i were inferred from time resolved spectra, which could account for the large difference between their observation and the present work. If Sanford et al.'s ion temperature measurements are truly representative of the radiating conditions in the pinch, they emphasis the lack of thermalization that is achieved when the radiation pulse is short. However, if the resolution of their spectrometer was inadequate to resolve a small line width, possibly approaching value obtained with the HY-Tech spectrometer, then the observed power radiated by the pinch cannot be resolved with calculated values obtained with a CRE model. [13] The model calculations require the reduced opacity of the higher ion temperatures to account for the radiated power. Measurements with a time resolved spectrometer having a high spectral resolution, such as the instrument developed in this program, are required to unambiguously resolve this discrepancy.

4.3 Radial Distribution of Electron Density and Temperature in a Z-pinch

The Si coated Al wire array shot DE4116 on Double Eagle described in Section 4.2.1 above was analyzed as a test case to evaluate the merits of inferring the radial distribution of the electron density and temperature from the ratio of supposedly optically thin lines. Three methods of analyzing the spectra are presented. The first approach utilizes the intensity ratios of the Ly_{α} to (He_{α} + IC) lines and the IC to He_{α} lines. This method led to a depressed value for the on-axis density, due to the opacity of the He_{α} line, and an unphysical increase in the electron density in the outer corona, which has been attributed to optical pumping of the resonance lines in the corona by resonance radiation from the core of the pinch. [2] The objective of the second approach was to see if the intensity of either the IC or He_{α} line can be used instead of the IC/ He_{α} line ratio as the density sensitive plasma parameter. Since the spectrometer was not absolutely calibrated, a normalization procedure was employed. For this purpose the density and temperature was determined at some radial position, r_0 , where neither opacity nor photon scattering are expected to be significant, and the IC/ He_{α} line ratio is therefore representative of the local density and temperature using the procedure in Method 1. These values for n_e and T_e were used to calculate the radiated intensity, which was use to normalize the intensity at all other radial positions. This led to a more realistic density profile but predicted an integrated line density greater than the initial load density. This is due, in part, to no criteria for choosing r_0 . The failure of the first two procedures led to the third where radiation transport through the plasma was used to fit the line-of-sight integrated intensity to the spatially resolved values of the Ly_{α} , He_{α} and IC lines. The procedures for doing these analyses are described below.

4.3.1 Determination of $n_e(r)$ and $T_e(r)$ by Method 1

The Si spectrum produced on Double Eagle in the short pulse by an Al wire array coated with 5% Si was recorded with a radially resolved Johann spectrometer. The radial profiles have not been corrected for the 150 μm spatial resolution of the imaging slits.

The Ly_α , He_α , IC and Li-like satellite lines of Si were spectrally averaged over the ion line profile and then Abel inverted to obtain the radial profiles of these lines shown in Figure 28. Since the Al He_δ and Si Ly_α lines were not spectrally resolved by the spectrometer, Gaussian functions were fit to the spectra at a number of radial positions to determine the relative fraction of the total intensity that is attributed to the Si Ly_α line. This is shown in Figure 29. The principal analytical tool which has been employed to infer electron density and temperature from measured line ratios is an ionization dynamics and radiation transport model of a one-dimensional (1D) cylindrical plasma containing detailed configurations atomic structure for the Li-, He, and H-like ionic stages of Al and Si. This model is described in more detail in Ref. 1. It includes all the important atomic collisional and radiative processes coupling the levels. To get accurate photoexcitation rates and to correctly calculate the self-absorption and power outputs, all optically thick lines are transported, as well as the two free-bound continua arising from radiative recombination to the K-shell ground states. The model solves for the steady-state populations of the individual levels assuming collisional-radiative equilibrium (CRE). The density and temperature required to produce a specific line ratio are then determined. These are shown as iso contours in Figure 30 for the $\text{Ly}_\alpha/\text{He}_\alpha + \text{IC}$ line ratio and in Figure 31 for the $\text{IC}/\text{He}_\alpha$ line ratio. The $\text{IC}/\text{He}_\alpha$ contours tend to be vertical for Si ion densities $\geq 10^{17}/\text{cm}^3$ making them highly density sensitive. The intersection of these contours for specific experimental values of each line ratio determines a value for n_e and T_e . This is then repeated for the line ratios at each radial position to yield the density and temperature profile shown in Figure 32.

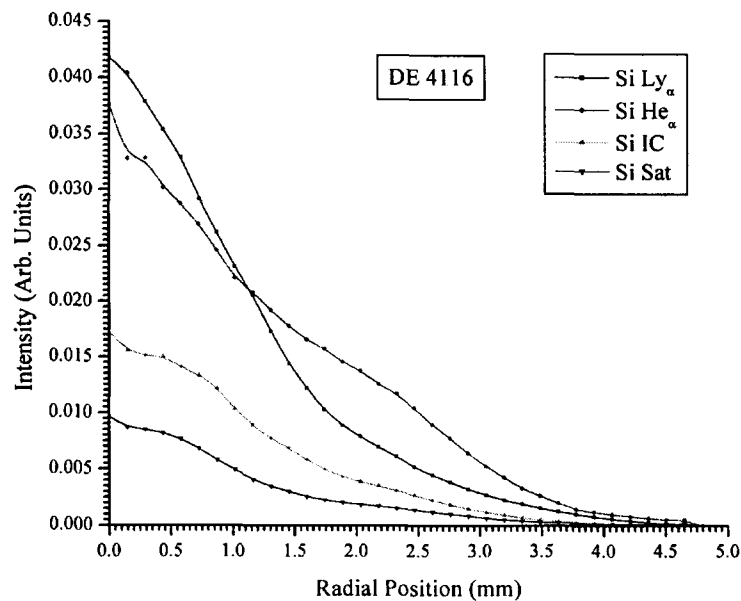


Figure 28. Radial distribution of the Abel inverted intensities (integrated over the ion line profile) of prominent resonance lines of Si and the jkl satellites. The order of the lines listed corresponds to their on-axis intensity.

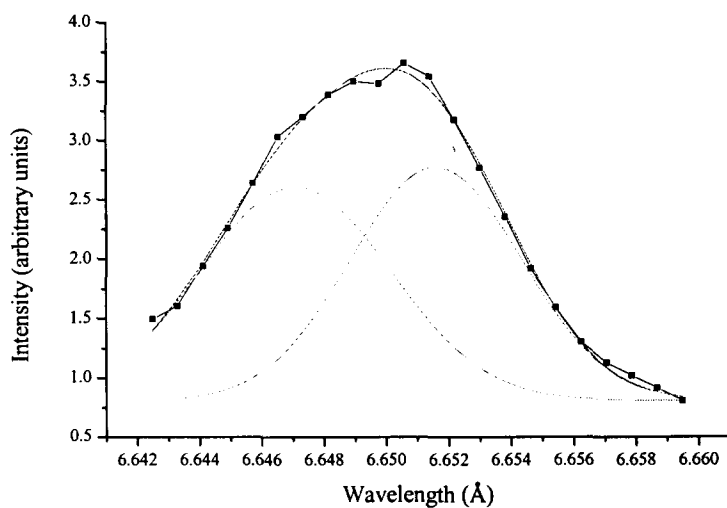


Figure 29. Fit to the observed line profile at $r=0$ by two Gaussian functions representing the Al He $_{\delta}$ line at 6.1745 Δ and the Si Ly $_{\alpha}$ at 6.180 Δ . The Si Ly $_{\alpha}$ intensity is found to be 0.45 of the total.

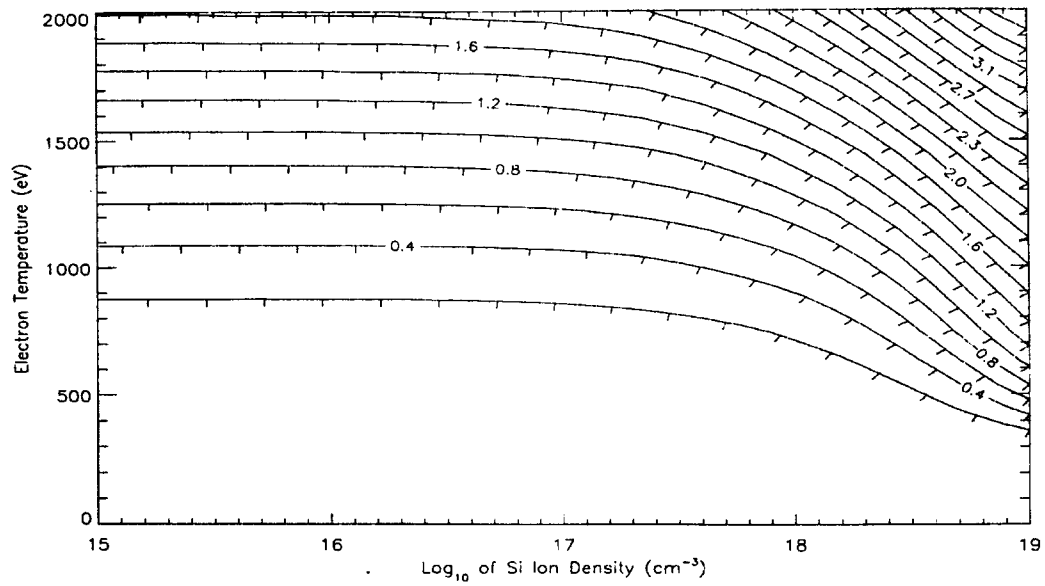


Figure 30. Calculated iso contours of the Ly_α to $(\text{He}_\alpha + \text{IC})$ line ratio for Si ions are shown as a function of the electron temperature and Si ion density for a 3 mm diameter cylindrical plasma composed of 95% Al and 5% Si.

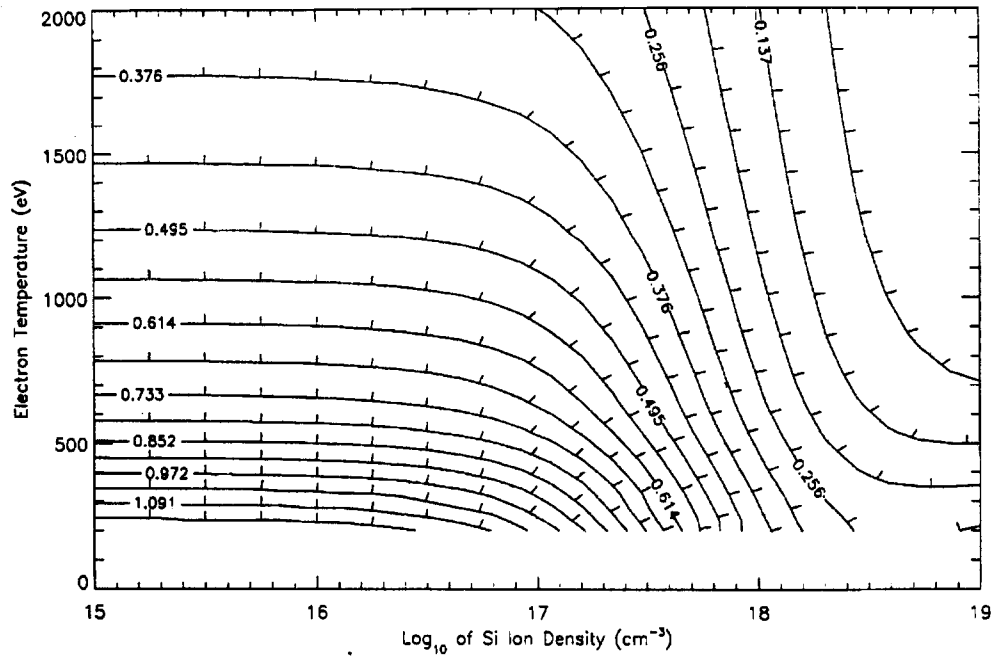


Figure 31. Calculated iso contours of the IC to He_α line ratio for the He-like Si ion are shown as a function of the electron temperature and Si ion density for a 3 mm diameter cylindrical plasma compound of 95% Al and 5% Si.

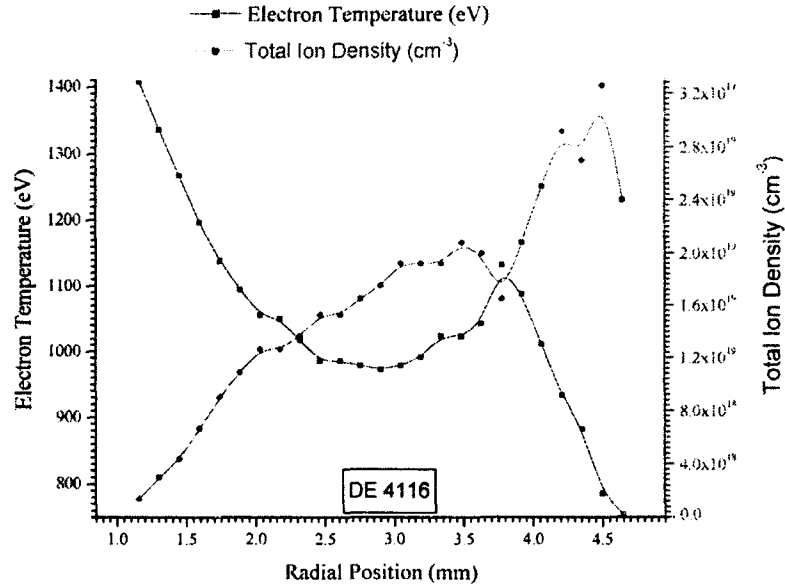


Figure 32. Radial distribution of electron temperature (square) and total ion density (dots) inferred from intersection of $\text{Ly}_\alpha/\text{He}_\alpha$ + IC and IC/ He_α contours.

The inferred density profile rises from a minimum value on axis to peak value at $r = 4.5$ mm. This distribution is counter intuitive since the distribution is assumed to decrease radially from a peak value on axis. This dip in the middle is due to opacity of the He_α line, which increases the IC/ He_α line ratio. The increase at the edges is attributed to absorption and re-emission (scattering) of radiation from the core of the pinch by He_α ions in the corona. This problem was thoroughly analyzed by Apruzese et al. [2] Their analysis shows that the He_α resonance level is populated twice as often by photo excitation in the edge of the plasma column as by collisional excitation where as radiative excitation of the intercombination line's ^3P upper level is at most a 1% effect. The combination results in a depressed value for IC/ He_α which is consistent with the high coronal ion density shown in Figure 32. The incorporation of this scattering affect in the spectral analysis is discussed in Section 4.3.3.

4.3.2 Determination of $n_i(r)$ and $T_e(r)$ Using the He_α or IC Intensity Profile

The ion density in Figure 32 is underestimated on-axis due to opacity effects and overestimated in the corona due to scattering. If an intermediate position, r_o , could be identified where neither opacity effects nor photon scattering significantly affects the IC/ He_α line ratio, then the ion density $n_i(r_o)$ and temperature $T_e(r_o)$ can be inferred at that location using the above method. The CRE model can then be used to predict the power radiated by the He_α or IC line at r_o . This value of $\text{He}_\alpha(r_o)$ could then be used to normalize the intensity at all other radial positions. The values of $n_i(r)$ and $T_e(r)$ can then be inferred at all other locations using the $\text{Ly}_\alpha/\text{He}_\alpha + \text{IC}$ line ratio and the line intensity.

The normalization point was chosen to be $r_o = 2$ mm. The resulting distributions of $n_i(r)$ and $T_e(r)$ are shown in Figure 33. The density distribution is seen to decrease monotonically from a peak value on axis. This is more physical than the distribution shown in Figure 32 where the density increases radially. However, the total number of radiating ions/units length that is calculated from this radial profile is about 1.5 times the number in the initial wire load, which clearly shows that this approach has major problems also. Since the density decreases as r approaches zero in Figure 32 it is clear that a smaller value of total ion density would have been obtained if r_o was chosen to be less than 2 mm. Unfortunately, this approach is not productive unless a criterion for choosing r_o can be identified.

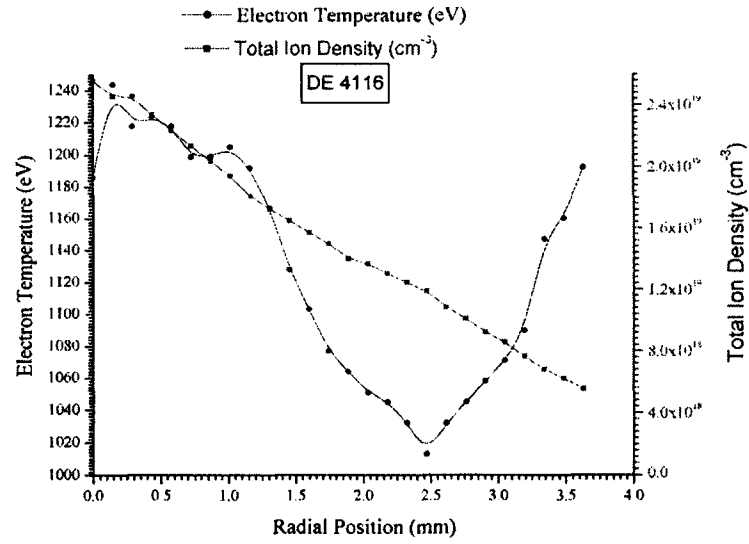


Figure 33. Radial distribution of electron temperature (dots) and total ion density (squares) inferred from intersection of $\text{Ly}_\alpha/\text{He}_\alpha + \text{IC}$ and He_α intensity contours normalized to n , T_e value at $r=2$ mm in

4.3.3 Alternate Approach to Inferring Radial Density and Temperature Profiles

The above example demonstrates the challenge of using the $\text{Ly}_\alpha/\text{He}_\alpha + \text{IC}$ line ratio and either the $\text{IC}/\text{He}_\alpha$ line ratio or the IC intensity to determine the radial density and temperature profile using Abel inverted spectral line intensities if either opacity or scattering of resonance radiation from the interior of the pinch are affecting the local population of upper states of the transitions studied. This has led to the method described below which calculates the spatial profiles of the spectral lines. This description draws heavily from the more complete presentation in reference [2].

The CRE calculation of J. Apuzese [1] that produced the contours shown in Figure 30 and 31 and used in the first two methods determined the intensities of the spectral lines, averaged over the pinch cross section. The spatially resolved spectra that will be used by this third method are determined by calculating the intensity I of an x-ray line emergent along a chord perpendicular to the pinch axis which is given by $I = (A_{ul}/R_c)h\nu \int_{\text{chord}} N_{ul}(s)P_e(s)ds$ where A_{ul} is the spontaneous decay rate for the transition, N_{ul} is the upper level population density as a function of the distance, s , along the chord, and $P_e(s)$ is the line escape probability for a Voigt profile. This aspect of the model

calculation is carried out for 41 chords whose impact parameters range from $r=0$ (intersecting the axis) to within 1.5% of the outer radius of the pinch.

Use of the calculated K-shell spectrum to fit the data (intensities, line ratios, powers, spatial profiles) is similar to that described in the first two methods. In the present case the assumed temperature and density profiles are iterated, typically requiring dozens to hundreds of separate calculations to find the best fit. Initially, simple but versatile analytic forms for the profiles are adopted, such as power laws or generalized Gaussians. As the calculations approach the data, hand adjustments of the profiles based on the observed variable sensitivities are made to fine tune the spectrum and zero in on an optimum fit. Based on the number of calculations, and the fact that similar but not identical profiles degrade the agreement with the data, we believe that the fits are unique in the sense that no profile differing significantly from the one deduced could fit the data as well. However, they cannot be proven to be so.

The temperature and density profiles which are employed to reproduce the line ratios and intensities of the data are shown in Figure 34. Note from the dotted lines of Figure 34 that both the Si line ratios and intensity profiles predicted by the model lie within the estimated experimental uncertainty of 15%. The electron density profile, when translated into Si and Al ion densities, accounts for only 40% of the initial mass load. The gentle decline in electron temperature shown in Figure 34 from 1.24 to 1.04 keV, axis to outer edge is required to replicate the gradual decline in the measured temperature sensitive $Ly_{\alpha}/(He_{\alpha} + IC)$ ratio shown in Figure 30. This analysis can be used to determine only the inner K-shell core conditions of the pinch, as a cooler outer halo exists which emits only the softer L-shell component of the total x-ray output. The decline in temperature and density with increasing radius is also consistent with the observed decrease of the intensity of the $(He_{\alpha} + IC)$ lines. What is initially puzzling and apparently paradoxical is the decrease in density with radius, despite the concurrent decrease of the IC/He_{α} ratio.

According to the standard theory outlined above in Sec. 4.3.1 and Figure 31, a decreasing line ratio should indicate increasing density.

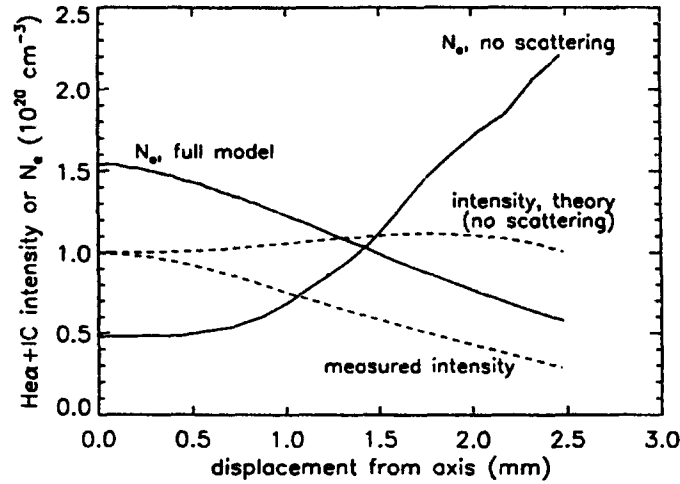


Figure 34. The electron density inferred when photoexcitation is neglected, and the ($\text{He}_\alpha + \text{IC}$) intensity profile predicted from this inferred density are plotted vs displacement from the axis. Also shown are the electron density obtained from the full model as well as the measured ($\text{He}_\alpha + \text{IC}$) intensity profile.

The explanation of this surprising result is the presence of intense line radiation from the core combined with the drastically differing absorption cross sections of the resonance and inter-combination lines. The upper levels of both lines are competitively populated by collisional excitation, and also by radiative excitation by the flux of line photons emitted from the hotter, denser pinch interior. The collisional excitation coefficients of both lines drop sharply with decreasing electron temperature, and in the outer regions of the K-shell emitting core, radiative excitation becomes increasingly dominant for the resonance line, as is shown in Figure 35. Note that, at the outer edge, the He_α resonance line is populated twice as often by photoexcitation as by collisional excitation. However, as also shown in Figure 35, radiative excitation of the intercombination line's ^3P upper level is at most a 1% effect. This is a straightforward consequence of the fact that the photoexcitation cross section of the intercombination line is less than that of the resonance line by a factor of 230. With increasing radius, resonance line emission is increasingly photoexcited by the flux of x-rays from the hotter, denser interior whereas this population mechanism is not available to the intercombination line. Thus, only the

spatially resolved intensity of the resonance line is enhanced by this scattering mechanism, reducing the IC/resonance ratio even though the electron density is decreasing.

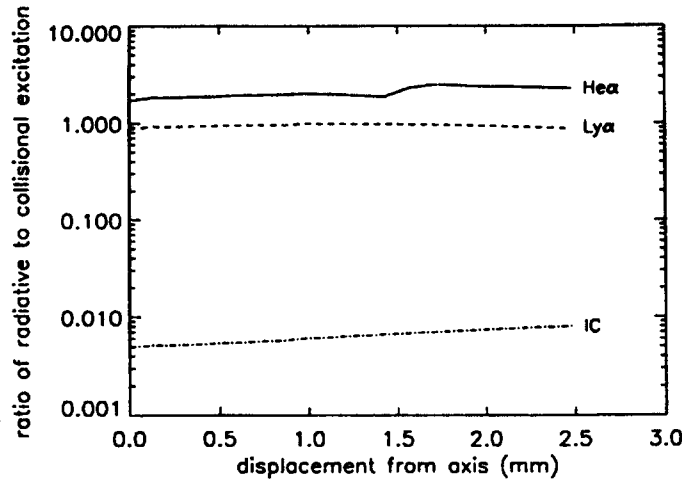


Figure 35. The ratio of radiative to collisional excitation is plotted for the profiles of Figure 33, for the $\text{Ly}\alpha$, $\text{He}\alpha$, and intercombination lines of K-shell Si ions.

Failure to properly take this mechanism into account can lead to the erroneous and seriously misleading density inferences obtained by Method 1. Figure 34 shows the electron density profile that is derived from the observed IC/resonance line ratio when x-ray scattering is neglected. Note that the density increases with radius just as in Figure 32, in accord with the usual interpretation of this line ratio. When this erroneous density profile is used, the spatially resolved intensity of the $(\text{He}\alpha + \text{IC})$ lines is found to increase with increasing radius, as also plotted in Figure 34, and in contrast to the data.

The averages of the spatial density and temperature profile obtained here were compared with averages values obtained using spatially integrated intensities and the analysis routine in Ref. [1]. The spatially averaged analysis uses the measured K-shell power and pinch diameter together with a temperature dependent line ratio such as the $\text{Ly}\alpha/\text{He}\alpha + \text{IC}$ to infer an electron temperature and ion density. For this Double Eagle 4116 shot, this spatially averaged analysis yields a value of $1.4 \times 10^{19}/\text{cm}^3$ for the ion density and 0.98 keV for the electron temperature if the peak value for the experimentally radiated power

is used. These values are only in fair agreement with a density of $8.0 \times 10^{18}/\text{cm}^3$ and temperature of 1.15 keV which are obtained by spatially averaging over the profile in Figure 34. Better agreement is achieved if the average radiated power instead of the peak power is used to analyze these time-averaged spectra. In this case a value of $9.8 \times 10^{18}/\text{cm}^3$ is obtained for the ion density and 1.11 keV for the electron temperature.

4.3.4 Summary of Radial Density and Temperature Profile Measurements

An imaging diagnostic technique was sought to determine the radial profiles of the electron density and temperature in a z-pinch from radially resolved x-ray line intensities that are Abel inverted to provide a measure of the local emission rate. A CRE model would then relate the ratio of these line intensities to the local density and temperature. The original approach was based on the different collisional excitation and quenching rates of the He_α and IC lines of He like ions, making their line ratio sensitive to the electron density. Unfortunately, these two lines also have vastly different photo absorption rates leading to opacity and scattering processes that also can affect the IC/ He_α line ratios. The opacity effect was recognized, but it was always assumed that the plasma would be optically thin for r greater than some value r_0 . In this case, IC/ He_α could be used to analyze the temperature and density profile for $r > r_0$ and the values of n_e and T_e at r_0 could be used to calculate the intensity of the IC line at r_0 . This value of $I_{\text{IC}}(r_0)$ could be used to normalize the intensity of the IC line for $r < r_0$ and this intensity could be used, together with the $\text{Ly}_\alpha/(\text{He}_\alpha + \text{IC})$ ratio to determine the temperature and density profiles. Unfortunately, this work has shown that photons emitted by the hot core can be absorbed by ions in the coronal region altering the local population of the upper He_α state. This effect increases the intensity of the He_α line which leads to an erroneous over estimation of the electron density. In spite of these complications, Apruzese et al. [2] have shown that a CRE model which includes these opacity and scattering effects can be used to calculate the observed intensity profile. The predicted spectrum is sufficiently sensitive to

the assumed density and temperature profile that this procedure can be used to infer these profiles with a high degree of confidence in their uniqueness.

The analysis of Apruzese et al. [2] also shows that n_e and T_e predicted with scattering effects included agrees with values obtained when scattering is ignored at some value of r as can be seen in Figure 34. Unfortunately the analysis does not provide a criterion for choosing this point. This single point might expand into a larger region near the center of pinch if the plasma is optically thin there. This possibility needs further analysis.

Appendix A

Bibliography

J. P. Apruzese, K. G. Whitney, J. Davis, and P. C. Kepple, "K-Shell line ratios and powers for diagnosing cylindrical plasmas of Ne, Al, Ar and Ti," J. Quant. Spectrosc. Radiat. Transf. 57, 41 (1997). (UNCLASSIFIED)

J. P. Apruzese, J. Davis, K. G. Whitney, E. J. Yadlowsky, E. P. Carlson, J. Niemel, F. Barakat, R. C. Hazelton, C. C. Klepper, J. J. Moschella, B. H. Failor, J. S. Levine, J. C. Riordan, Y. Song, and B. L. Whitton, "Analyzing spatially resolved line spectra emitted by Z pinches," Phys. Plasmas 7, 3399 (2000). (UNCLASSIFIED)

S. H. Glenzer, C. A. Back, K.G. Estabrook, B. J. MacGowan, D. S. Montgomery, R. K. Kirkwood, J. D. Moody, D. H. Munro, and G. F. Stone, "Electron temperature and density measurements in laser-produced large-scale-length gas bag plasmas by x-ray spectroscopy," Phys. Rev E 55, 927 (1997). (UNCLASSIFIED)

C. De Michelis and M. Mattioli, "Soft x-ray spectroscopic diagnostic of laboratory plasmas," Nuclear Fusion 21, 677 (1981). (UNCLASSIFIED)

J. Dubau, M. K. Inal, and A. M. Lerner, "Diagnostics of the anisotropy of the electron distribution from the analysis of x-ray line polarization," Physica Scripta T65, 179 (1996). (UNCLASSIFIED)

H. R. Griem, Plasma Spectroscopy, McGraw-Hill, New York (1964). (UNCLASSIFIED)

R. U. Datla and H. R. Griem, "Stark profile measurements on Lyman series lines of Al_{XIII}," Phys. Fluid 21, 505 (1978). (UNCLASSIFIED)

K. L. Wong, P. T. Springer, J. H. Hammer, C. A. Inglesias, A. L. Osterheld, M. E. Foord, H. C. Bruns, J. A. Emig, and C. Deeney, "Spectroscopic characterization of an argon-neon z-pinch plasma at stagnation," Phys. Rev. Letters 80, 2334 (1998). (UNCLASSIFIED)

B. A. Hammel, D. W. Phillion, and L. E. Ruggles, "Demonstrating of reduced source size broadening with a Johann focusing elliptical spectrometer and theory of the second order source broadening," Rev. Sci Instrum. 61, 1920 (1990). (UNCLASSIFIED)

P. Berensdorfer, S. von Goeler, M. Bitter, K. W. Hill, R. A. Hulse, and R. S. Walling, "High-resolution bent-crystal spectrometer for the ultra soft x-ray region," Rev. Sci Instrum. 60, 895 (1989). (UNCLASSIFIED)

K. L. Wong, P. T. Springer, H. C. Bruns, J. A. Emig, J. H. Hammer, A. L. Osterheld, and C. Deeney, "Spectroscopic characterization of an argon-neon plasma at stagnation", 37th Annual Meeting of the Division of Plasma Phys., APS, Nov. 6-10 (1995). (UNCLASSIFIED)

T. W. L. Sanford, T. J. Nash, R. C. Mock, R. B. Spielman, K. W. Stuve, J. H. Hammer, J. S. De Groot, K. G. Whitney, and J. P. Apruzese, "Dynamics of a high-power aluminum – wire array z-pinch implosion," *Phy of Plasmas* 4, 2188 (1997). (UNCLASSIFIED)

J. Apruzese, Private communication. (UNCLASSIFIED)

B. L. Henke, E. M. Gullikson, and J. C. Davis, "X-ray Interactions: Photo absorption, Scattering, Transmission, and Reflection $E=50\text{-}30,000$ eV, $Z=1\text{-}92$," Lawrence Berkeley Laboratory report LBL-33908 (1993). (UNCLASSIFIED)

N. A. Dyson, X-Rays in Atomic and Nuclear Physics, 2nd edition, Cambridge University Press, Cambridge, 1990 p. 79. (UNCLASSIFIED)

M. A. Blokhin, Methods of X-ray Spectroscopic Research, Pergamon Press, Oxford, 1965 p. 420. (UNCLASSIFIED)

R. L. Kelly, Atomic and Ionic Spectrum Lines below 2000\AA , ORNL-5922 (1982). (UNCLASSIFIED)

**DISTRIBUTION LIST
DTRA- TR -01-21**

DEPARTMENT OF DEFENSE

DEFENSE ADVANCED RESEARCH PROJECT
AGENCY
3701 NORTH FAIRFAX DRIVE
ARLINGTON, VA 22203-1714
ATTN: DED
ATTN: MTO/J. ZOLPER
ATTN: SP/M. OBLE

DEFENSE THREAT REDUCTION AGENCY
8725 JOHN J. KINGMAN ROAD, STOP 6201
FT BELVOIR, VA 22060 - 6201
ATTN: TD/ D. LINGER
ATTN: TDN/COL M. DONOVAN
ATTN: TDNA/R. DAVIS

DEFENSE THREAT REDUCTION AGENCY
ALBUQUERQUE OPERATIONS
1680 TEXAS STREET SE
KIRTLAND AFB, NM 87117-5669
ATTN: TDTD/ G. LU
5CYS ATTN: TDTDN.D. BALL

DOT&E TEST AND EVALUATION CENTER
2001 NORTH BEAUREGUARD STREET
SUITE 800
ALEXANDRIA, VA 22311
ATTN: DOT&E/D. HINTON
ATTN: DOT&E/R. MANRIQUEZ

DoD MISSILE DEFENSE AGENCY
7100 DEFENSE PENTAGON
WASHINGTON, DC 20301 - 7100
ATTN: ST/C. INFOSINO
ATTN: TER/J. MCCOMB

DoD MISSILE DEFENSE AGENCY
JOINT PROGRAM OFFICE (NMD-JPO)
1725 JEFFERSON DAVIS HIGHWAY,
SUITE 12021
ARLINGTON, VA 22202-4102
ATTN: E. HUDAK

DoD MISSILE DEFENSE AGENCY
JOINT PROGRAM OFFICE (JPO)
P.O. BOX 1500
ARLINGTON, VA 35807-3801
ATTN: JN1-EH/D. PIERCE

DEFENSE
TECHNICAL INFORMATION CENTER
8725 JOHN J. KINGMAN ROAD, SUITE 0944
FORT BELVOIR, VA 22060 - 6218
2 CYS ATTN: DTIC/OCA

DEPARTMENT OF THE ARMY

US ARMY NUCLEAR AND CHEMICAL
AGENCY
7150 HEELER LOOP, SUITE 101
SPRINGFIELD, VA 22150 - 3198
ATTN: ATNA-ZA/C. DAVIDSON
ATTN: AD LIBRARY

ARMY RESEARCH LABORATORIES
2800 POWDER MILL ROAD
ADELPHI, MD 20783-1197
ATTN: AMSRD-ARL-SE/J.
PELLEGRINO
ATTN: AMSRD-ARL-SE-DP/
S.SCOZZIE

ARMY SPACE AND MISSILE DEFENSE
TECHNICAL CENTER
P.O. BOX 1500
HUNTSVILLE, AL 35807
ATTN: SMDC-TC-WV/P. SIMPSON

ARMY TEST AND EVALUATION COMMAND
4501 FORD AVENUE
ALEXANDRIA, VA 22302
ATTN: TECHNICAL DIRECTOR/
B. BARR

WHITE SANDS MISSILE RANGE
DEPARTMENT OF THE ARMY
NUCLEAR EFFECTS DIVISION
WHITE SANDS, NM 88002 - 5176
ATTN: STEWS-NE/J. MEASON

DEPARTMENT OF THE NAVY

OFFICE OF NAVAL RESEARCH
800 NORTH QUICNY STREET
ARLINGTON, VA 22217 - 5660
ATTN: CODE 31/K.HATHAWAY
ATTN: CODE 33/R. POHANKA

**DISTRIBUTION LIST
DTRA-TR- 01-21**

NAVAL RESEARCH LABORATORY
4555 OVERLOOK AVENUE, SW
WASHINGTON, D.C. 30375-5000
ATTN: CODE 6700/S. OSSAKOW
ATTN: CODE 6720/J.DAVIS
ATTN: CODE 6720/W. THORNHILL
ATTN: CODE 6720/J. APRUZESE
ATTN: CODE 6770/G. COOPERSTEIN
ATTN: CODE 6770/R. COMMISSO
ATTN: CODE 6370/G. HUBLER

NAVAL SURFACE WARFARE CENTER
DAHLGREN DIVISION
11720 DAHLGREN ROAD
DAHLGREN, VA 22448- 5100
ATTN: CODE G23/J. PARTAK
ATTN: TECHNICAL LIBRARY

NAVAL SURFACE WARFARE CENTER
CARDEROCK DIVISION
9500 MACARTHUR BOULEVARD
WEST BETHESDA, MD 20817-5700
ATTN: CODE 682/R.STARK

NAVAL STRATEGIC SYSTEMS PROGRAMS
REENTRY SYSTEMS BRANCH
NEBRASKA AVENUE COMPLEX
287 SOMERS COURT NW
WASHINGTON, DC 20393-5446
ATTN: SP28/B. HANNA

DEPARTMENT OF THE AIR FORCE

AIR FORCE OPERATIONAL TEST AND
EVALUATION CENTER
8500 GIBSON BOULEVARD, SE
ALBUQUERQUE, NM 87117
ATTN: AFOTEC CN.M. WILLIAMS

AIR FORCE RESEARCH LABORATORY
1950 5TH STREET, BLDG 18
WRIGHT PATTERSON AFB, OH 45433 - 7251
ATTN: PRP/LT.COL J. ERNO
ATTN: PRPE/J. SCOFIELD

AIR FORCE RESEARCH LABORATORY
3550 ABERDEEN AVENUE, SE
KIRTLAND AFB, NM 87117 - 5776
ATTN: DEHP/J. DEEGAN
ATTN: DEHP/G. KIUTTU

AF SPACE AND MISSILE CENTER
2420 VELA WAY
SUITE 1467/A8
EL SEGUNDO, CA 90245- 4687
ATTN: SMC/XR/COL W. GARDNER

ARNOLD ENGINEERING DEVELOPMENT
CENTER
100 KINDEL DRIVE
ARNOLD AFB, TN 37389- 1214
ATTN: AEDC/CD/A. GOLDSTAYN
ATTN: AEDC/XPV/B. STEWART

ARNOLD ENGINEERING DEVELOPMENT
CENTER
1099 AVENUE C, SUITE 106R
ARNOLD AFB, TN 37389-9010
ATTN: AEDC/DOR/R.POLCE

ARNOLD ENGINEERING DEVELOPMENT
CENTER
1088 AVENUE C
ARNOLD AFB, TN 37389- 6700
ATTN: AEDC/DOS/CAPT.N.TRACEY

ICBM SYSTEM PROGRAM OFFICE
REENTRY SYSTEMS DIVISION
6011 GUM LANE
HILL AFB, UT, 84056
ATTN: OO-ALC-LMR/A. JEX

DEPARTMENT OF ENERGY

UNIVERSITY OF CALIFORNIA
LAWRENCE LIVERMORE NATIONAL
LABORATORY
P.O. BOX 808
LIVERMORE, CA 94551 - 9900
ATTN: REPORTS LIBRARY

LOS ALAMOS NATIONAL LABORATORY
P.O. BOX 1663
LOS ALAMOS, NM 87545
ATTN: REPORTS LIBRARY

**DISTRIBUTION LIST
DTRA-01-21**

SANDIA NATIONAL LABORATORIES

ATTN: MAIL SERVICES

P.O. BOX 5800

ALBUQUEURQUE, NM 87185- 0459

ATTN: C. DEENEY, MS 1194

ATTN: C. COVERDALE, MS 1159

ATTN: M. HEDEMAN, MS 1159

ATTN: D. MCDANIEL, MS 1194

ATTN: REPORTS LIBRARY

DEPARTMENT OF DEFENSE CONTRACTORS

ALAMEDA APPLIED SCIENCES CORPORATION

626 WHITNEY STREET

SAN LEANDRO, CA 94577

ATTN: M. KRISHNAN

ATTN: P. COLEMAN

ATTN: J. THOMPSON

ALME AND ASSOCIATES

6020 SOUTH RICHMOND HWY #204

ALEXANDRIA, VA 22303

ATTN: J. DAVIS

ATTN: S. SEILER

AEROSPACE TESTING ALLIANCE

AEDC GROUP

1088 AVENUE C

ARNOLD AFB, TN 37389 - 6700

ATTN: T. COTTER

ATTN: V. KENYON

ATTN: J. STEELE

AVONIA

13631 OLD EL CAMINO REAL

SAN DIEGO, CA 92130

ATTN: A. WILSON

BERKELEY RESEARCH ASSOCIATES

6551 MID CITIES AVENUE

BELTSVILLE, MD 20075-1434

ATTN: J. ORENS

ECOPULSE, INC.

P.O. BOX 528

SPRINGFIELD, VA 22150

ATTN: N. PEREIRA

HY-TECH RESEARCH CORPORATION

104 CENTRE COURT

RADFORD INDUSTRIAL CENTER

RADFORD, VA 24141

ATTN: E. YADLOWSKY

ATTN: R. HAZELTON

ATTN: J. MOSCHELLA

ITT INDUSTRIES

ITT SYSTEMS CORPORATION

1680 TEXAS STREET SE

KIRTLAND AFB, NM 87117 - 5669

ATTN: DTRIAC

2 CYS ATTN: DTRIAC/DARE

ITT INDUSTRIES

2560 HUNTINGTON AVENUE

ALEXANDRIA, VA 22303

ATTN: R. BRENINGER

ITT INDUSTRIES

P.O. BOX 15012

COLORADO SPRINGS, CO 80935 - 5012

ATTN: M. LYNCH

ATTN: T. STRINGER

KTECH CORPORATION

2201 BUENA VISTA, SE

ALBUQUERQUE, NM 87106 - 4265

ATTN: F. DAVIES

ATTN: D. LEPELL

**NORTHROP GRUMMAN INFORMATION
TECHNOLOGY**

2100 WASHINGTON BOULEVARD

ARLINGTON, VA 22204

ATTN: I. VITKOVISKY

NUMEREX

2309 RENARD PLACE, SUITE 220

ALBUQUERQUE, NM 87106 - 4259

ATTN: M. FRESE

SCIENCE RESEARCH LABORATORY, INC.

15 WARD STREET

SOMERVILLE, MA 02143

ATTN: J. JACOB

TITAN PULSE SCIENCES DIVISION

2700 MERCED STREET

SAN LEANDRO, CA 94577-0599

4 CYS ATTN: P. SINCERNY

ATTN: H. SZE